Earth-Science Reviews 250 (2024) 104681

Contents lists available at ScienceDirect

Earth-Science Reviews

journal homepage: www.elsevier.com/locate/earscirev

Review Article

Mercury stable isotopes revealing the atmospheric mercury circulation: A review of particulate bound mercury in China

Xuechao Qin [a,b,e], Qingjun Guo [a,d,*], Pim Martens [c], Thomas Krafft [b]

[a] Institute of Geographic Sciences and Natural Resources Research, Chinese Academy of Sciences, Beijing 100101, China
[b] Department of Health, Ethics and Society, Care and Public Health Research Institute, Faculty of Health, Medicine and Life Sciences, Maastricht University, 6229 HA Maastricht, the Netherlands
[c] System Earth Science/University College Venlo, Maastricht University, Nassaustraat 36, 5911 BV Venlo, the Netherlands
[d] College of Resources and Environment, University of Chinese Academy of Sciences, Beijing 100190, China
[e] University of Chinese Academy of Sciences, Beijing 100049, China

ARTICLE INFO

Keywords:
Atmospheric mercury
Mercury isotopes
Mercury biogeochemical circulation
China
Machine learning

ABSTRACT

Human activities since industrialization have significantly raised global atmospheric mercury (Hg) levels. China's high Hg emissions with rapid industrial development have a global impact on implementing the Minamata Convention on Mercury due to the dispersion of atmospheric Hg. Here, we comprehensively reviewed the atmospheric particulate bound mercury (PBM) in China, given its highest deposition rate, aiming to elucidate Hg sources, transformation, and geochemical cycles. Firstly, we analyzed its spatiotemporal distribution and long-term trends in China by synthesizing published literature. Most of the studies were conducted in eastern China, where PBM concentrations are higher than in western China due to extensive anthropogenic emissions. Furthermore, meteorological factors and atmospheric transport significantly affect seasonal PBM variations. Local anthropogenic sources, atmospheric transport, and local atmospheric transformation contribute 56.2%, 14.9%, and 29.0% to China's PBM content, respectively. Notably, China's atmospheric PBM concentrations have declined significantly since 2015. Secondly, we compiled a comprehensive global Hg isotope dataset and employed structural equation modeling to quantify Hg geochemical cycling. The isotope ratios of atmospheric Hg primarily overlap with those of Hg raw materials and vegetation. The significant relationship ($P < 0.01$) between atmospheric Hg and Hg raw materials (0.91) and vegetation (1.78) suggests that they contribute significantly to atmospheric Hg. Besides water and fish, atmospheric Hg also shows a high regression coefficient with human Hg, raising concerns about direct human inhalation of atmospheric Hg. Thirdly, we combined compiled Hg isotopes with machine learning to predict PBM sources in China. Industrial activities, biomass burning, and soil/dust are the primary contributors to PBM in China, accounting for 58.67%, 22.11%, and 17.14%, respectively. Our findings indicate that the contribution of soil/dust to PBM, ranging from 0.51% to 56.42%, has been underrated in previous studies. It is feasible to trace atmospheric Hg transport using Hg isotopes, as PBM mainly undergoes photoreduction reactions, but quantifying regional Hg transport remains challenging.

1. Introduction

Mercury (Hg), a highly toxic heavy metal that can be transported globally, is mainly released into the atmosphere through human activities (e.g., metal smelting, coal burning) and natural emissions (Hg re-emissions from oceans and forests, etc.) (AMAP/UNEP, 2019). Atmospheric Hg transported globally with the circulation can enter terrestrial and aquatic ecosystems through dry and wet deposition, leading to the formation of highly toxic methylmercury under certain circumstances that pose a threat to human and other biological safety (Blanchfield et al., 2022; Driscoll et al., 2013; Obrist et al., 2018; Sonke et al., 2023). Human activities have caused a multifold increase in atmospheric Hg levels since industrialization (Streets et al., 2011). According to AMAP/UNEP (2019), human activities emitted approximately 2500 tons of Hg into the atmosphere in 2015, with industrial production accounting for approximately 27% and fossil fuel and biomass combustion accounting for approximately 24%. Multiple countries and organizations signed the Minamata Convention on Hg in 2013, aiming to reduce Hg emissions

* Corresponding author at: Institute of Geographic Sciences and Natural Resources Research, Chinese Academy of Sciences, Beijing 100101, China.
E-mail address: guoqj@igsnrr.ac.cn (Q. Guo).

https://doi.org/10.1016/j.earscirev.2024.104681
Received 1 August 2023; Received in revised form 28 December 2023; Accepted 15 January 2024
Available online 18 January 2024

from human activities through various measures, which officially entered into force in 2017. Gaseous elemental Hg (GEM), gaseous oxidized mercury (GOM), and particulate bound mercury (PBM), which are the three forms of atmosphere Hg, can undergo mutual conversion (Ariya et al., 2015). GEM is relatively stable, not easy to settle, and can stay in the atmosphere for around half a year (Horowitz et al., 2017). PBM and GOM have fast atmospheric deposition rates, typically remaining in the atmosphere for several days to weeks (Horowitz et al., 2017). They are the primary forms of atmospheric Hg deposition, especially PBM (GEM and GOM adsorbed in atmospheric aerosols can form PBM), which has the fastest deposition rate (Poissant et al., 2005). Identifying Hg sources and tracking atmospheric Hg transport is critical to determining Hg geochemical cycling and managing atmospheric Hg emissions.

There are seven stable isotopes of Hg, with natural abundances of ^{196}Hg (0.155%), ^{198}Hg (10.04%), ^{199}Hg (16.94%), ^{200}Hg (23.14%), ^{201}Hg (13.17%), ^{202}Hg (29.73%), and 204Hg (6.82%), respectively (Blum and Bergquist, 2007). The natural abundance of ^{196}Hg is relatively low, so it is rarely used in practice, and ^{198}Hg is used as the denominator for calculating the relative abundance of other isotopes (Text S1). Hg stable isotopes are divided into three fractionation methods: mass-dependent fractionation (MDF), δ^{202}Hg; mass-independent fractionation of odd Hg (odd-MIF), Δ^{199}Hg and Δ^{201}Hg; and mass-independent fractionation of even Hg (even-MIF), Δ^{200}Hg and Δ^{204}Hg (Blum et al., 2014). The degree of MDF is directly commensurate to the mass difference between isotopes. Many physicochemical and biological processes can lead to MDF of Hg stable isotopes, such as diffusion, volatilization, oxidation, reduction, methylation, etc. (Bergquist and Blum, 2007; Estrade et al., 2009; Perrot et al., 2013; Smith et al., 2015; Zheng and Hintelmann, 2009). According to the current research, the odd-MIF is caused by the nuclear volume effect (NVE) and magnetic isotope effect (MIE), triggered mainly by the photochemical process. For instance, photochemical reduction of Hg (II) (Bergquist and Blum, 2007; Rose et al., 2015; Zheng and Hintelmann, 2009), photodemethylation (Kritee et al., 2018), and photooxidation (Liu et al., 2022a; Sun et al., 2016a) can all generate significant odd-MIF. However, the formation mechanism of even-MIF is still unclear. Since even-MIF mainly exists in atmospheric Hg samples and other samples affected by atmospheric deposition, its formation is likely associated with atmospheric Hg's redox process in the troposphere (Blum and Johnson, 2017; Cai and Chen, 2016; Fu et al., 2021a). For example, Chen et al. (2012) observed significant even-MIF of Hg isotopes (up to 1.24‰ for Δ^{200}Hg) in atmospheric snow and rain samples from North America. Different substances and reaction processes drive Hg to exhibit different Hg isotopic compositions. The three fractionations above make Hg isotopes a unique "three-dimensional" isotope system, assembling stable Hg isotopes as an ideal method for tracing Hg sources, transformation, and geochemical cycles.

Due to rapid industrial development, China has been regarded as a country with high Hg emissions worldwide, representing approximately 26.0% in 2015 (AMAP/UNEP, 2019; Steenhuisen and Wilson, 2019). However, significant reductions in atmospheric Hg concentrations have also been observed in China in recent years (Fu et al., 2015; Tang et al., 2018). The global dispersion of atmospheric Hg makes China's emissions have a significant impact on the world. Therefore, understanding the atmospheric Hg situation in China is of great significance for global Hg environmental safety and the implementation of the Minamata Convention on Mercury. This article selects China's PBM as the research object, given the rapid deposition and circulation of PBM and relatively severe aerosol pollution in China (Huang et al., 2014; Liu et al., 2022b). First, we analyzed the spatiotemporal distribution and long-term trends of PBM in China based on the collected data from published literature. Secondly, we compiled a Hg isotope dataset encompassing various sources from published papers and employed structural equation modeling (SEM) to determine the geochemical circulation of Hg. Finally, we highlighted combining machine learning (random forest model) and the compiled Hg isotope dataset to predict atmospheric Hg sources (here, PBM) and discussed Hg transport in China. Our research is geared towards comprehensive insights into the atmospheric Hg distribution, sources, transport, and circulation.

2. Materials and methods

2.1. Mercury isotope and China PBM content data collection

Both Hg isotope data and China's PBM content data were derived from peer-reviewed papers on the Web of Science. The collected global Hg isotope data sources are shown in Fig. 4, divided into 22 categories, with over 4000 Hg isotope samples, of which the number of δ^{202}Hg, Δ^{199}Hg, Δ^{200}Hg, and Δ^{201}Hg data are 4316, 4281, 3443, and 4210, respectively. Using the subject heading (atmospheric Hg) and manual screening, we collected 56 studies on PBM concentrations in China, published from 2001 to 2022, including 110 sites in China. Detailed PBM information is shown in Table S1. The sampling method of atmospheric PBM samples meets either active sampling (Tekran 2537 system) or passive sampling (air sampler plus filter membrane).

2.2. Principal component analysis-multiple linear regression

We extracted the average monthly PBM concentration data from each site from published papers (Table S1) and combined it with the other gridded atmospheric data of China (Tang et al., 2021) to conduct a traceability analysis using principal component analysis-multiple linear regression (PCA-MLR, Text S2). The gridded atmospheric data includes meteorological data (x-wind component, Y-wind component, surface temperature, surface relative humidity, surface pressure) and common atmospheric pollutant data (CO, O_3, SO_2, NO_2, PM_{10}, $PM_{2.5}$), with a horizontal resolution of 15 km and covering the period from 2013 to 2019. We selected this dataset as the Chinese government began large-scale monitoring and disclosure of atmospheric air quality data after 2013, and most atmospheric Hg monitoring was carried out before 2020.

2.3. Structural equation modeling

SEM is widely used as a multivariate data analysis method to explore causal relationships between variables and measure models (Mardani et al., 2020; Xiong et al., 2015). SEM divides variables into observational and latent variables. Observational variables are attributes of latent variables, while latent variables cannot be directly measured but can be obtained through statistical analysis of measured values of multiple observational variables. Therefore, by establishing a mathematical model, it is possible to infer the causal relationship between various potential and observed variables. In this study, we used SEM to reveal the Hg geochemical cycles based on the Hg isotope compositions of natural materials. We took the Hg isotope values (δ^{202}Hg, Δ^{199}Hg) of each source as the observed variable and the corresponding Hg source as the latent variable, that is, using the measurable Hg isotope value to characterize each source. Then, the linear regression method was employed to explore the causal association between various Hg sources and reveal Hg geochemical cycles. We employed the "lavaan" package of R to implement SEM and took the covariance matrix to evaluate the model result (Rosseel, 2012).

2.4. Machine learning - random forest model

Given the increased complexity in tracing Hg emission sources due to their mixing, we adopted the random forest model (RFM) to predict the sources of PBM. RFM is an ensemble machine learning method that completes classification or regression tasks by building multiple decision trees. Its advantage is that RFM can reduce the risk of overfitting and handle a large number of features and data. We modeled Hg isotope

compositions of different emission sources using the random forest classifier (RFC) approach and used the trained model to predict atmospheric PBM sources. We took Hg isotope values (δ^{202}Hg, Δ^{199}Hg, and Δ^{200}Hg) of emission sources as feature values and source types (coal, lichens, etc.) as target values. The RFC object of the ensemble module of Python's sklearn package was employed in our study (Pedregosa et al., 2011). During model training, the bagging method was adopted for sample sampling, the information entropy method was taken to divide the nodes of the random forest decision tree, and finally, the out-of-bag estimation was employed to validate the trained model. Using the trained model, we predicted atmospheric PBM sources by employing Hg isotope values (δ^{202}Hg, Δ^{199}Hg, and Δ^{200}Hg) of PBM as inputs to determine the possibility of PBM belonging to various Hg emission sources.

3. Results and discussion

3.1. PBM concentrations across China

3.1.1. Spatial patterns

Given that most studies focus on Hg combined with $PM_{2.5}$ or TSP, Table S1 presents a statistical summary of observed PBM ($PBM_{2.5}$ and PBM_{TSP}) in China. The median concentrations of $PBM_{2.5}$ and PBM_{TSP} in China are 74.5 and 273.6 pg m^{-3}, ranging from 14.3 to 1330.0 and 23.5 to 1180.0 pg m^{-3}, respectively (Fig. S1A, 1B). A few studies have simultaneously observed both $PBM_{2.5}$ and PBM_{TSP} concentrations at the same sites, and the observed results show that the mean $PBM_{2.5}/PBM_{TSP}$ ratio is 56.4% ± 14.2%, ranging from 35.7% to 72.5% (Fig. S1C) (Qin et al., 2016; Schleicher et al., 2015; Yu et al., 2019). The first report of PBM observation in China published on the Web of Science was in 2001, and the observational experiment was conducted in 1999. Therefore, Fig. S1D and Fig. 1 divide the published PBM articles into two parts with 2010 as the boundary: before 2010 and after 2010. Both the $PBM_{2.5}$ and PBM_{TSP} concentrations decreased in China after 2010 compared with before 2010 (Fig. S1D). As shown in Fig. 1, more $PBM_{2.5}$ and PBM_{TSP} observation sites were conducted in China after 2010 than before 2010, especially for $PBM_{2.5}$, the number of observational sites increased dramatically. Moreover, most sites have been carried out in economically developed cities, such as the Beijing-Tianjin-Hebei region (BTH), the Yangtze River Delta, and the Pearl River Delta. Correspondingly, these developed cities in eastern China present higher $PBM_{2.5}$ and PBM_{TSP} concentrations (Fig. 1) and atmospheric Hg emissions (AMAP/UNEP, 2013; AMAP/UNEP, 2019) compared to western China.

Atmospheric PBM monitoring sites can be divided into five types, including remote/rural, suburban, urban, coastal, and island areas (Fig. S2). The mean PBM concentrations in these different regions are 91.6, 219.0, 241.6, 155.0, and 66.0 pg m^{-3}, with ranges of 14.3–516.7, 30.0–680.0, 19.4–1330.0, 16.3–210.0, and 16.6–230.0 pg m^{-3}, respectively. The variation of the median of PBM concentrations is similar to the mean PBM concentrations, with urban areas having the highest median concentration (182.8 pg m^{-3}), followed by suburban (131.2 pg m^{-3}), coastal (125.2 pg m^{-3}), remote/rural (49.0 pg m^{-3}), and island areas (27.0 pg m^{-3}). There are four rural/remote sites with PBM concentrations above 100 pg m^{-3}, all located in the Taklimakan desert, mainly because flying sand particles in deserts can act as carriers of atmospheric Hg to carry Hg for migration and deposition (Huang et al., 2020a).

3.1.2. Diel variations

The diurnal variations of PBM concentrations vary between daytime and nighttime. Some studies have found that there is no significant difference in the PBM concentrations between daytime and nighttime, such as in urban Beijing (Wang et al., 2021b; Zhang et al., 2019), urban Guiyang (Liu et al., 2011), remote Tibetan Plateau (Zhang et al., 2015), and Mt. Changbai (Lin et al., 2019). However, significant variations of PBM concentration are also observed between day and night in other studies, with higher PBM concentrations at night than during the day (Duan et al., 2017b; Huang et al., 2019). In contrast, Fu et al. (2012) reported that the PBM concentration at Mt. Waliguan in northwestern China was higher during the day than at night, possibly due to the effect

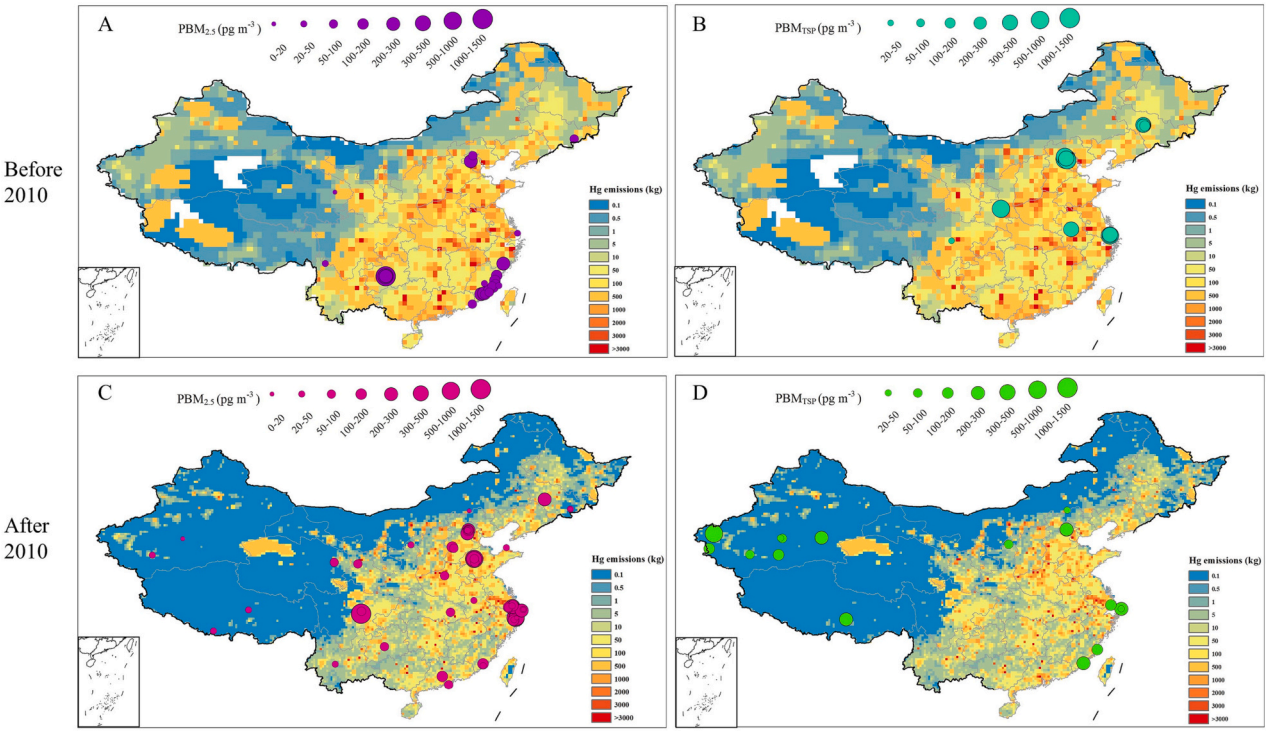

Fig. 1. Spatial and temporal patterns of $PBM_{2.5}$ and PBM_{TSP} concentrations in mainland China before 2010 (A, B) and after 2010 (C, D). The dots represent the observational sites from published articles (Table S1), and the 0.5° × 0.5° grided anthropogenic Hg emissions in 2010 (A, B) and 2015 (C, D) in mainland China are from AMAP/UNEP, 2013, 2019.

of long-range transport and regional emissions. Schleicher et al. (2015) also found that PBM concentrations in urban Beijing were generally higher at nighttime than in daytime in summer, while PBM levels were usually higher during the day in other seasons. The variations in PBM concentrations between daytime and nighttime are likely attributed to regional emissions and meteorological conditions rather than differences in sampling sites. For instance, during nighttime, lower wind speeds and a reduced atmospheric boundary layer, coupled with higher relative humidity compared to daytime, facilitate the conversion of GOM or GEM into PBM (Lee et al., 1998; Liu et al., 2007; Nair et al., 2012; Qin et al., 2019). Additionally, these conditions limit the vertical exchange of atmospheric airflow, contributing to PBM accumulation.

Although the difference between total daytime and nighttime PBM contents is variable, most studies have found distinct hourly sequence changes in PBM concentrations. The diurnal variations of atmospheric PBM concentrations in remote areas differ from other regions, such as rural, suburban, urban, and coastal regions (Table S2). In remote areas, PBM concentrations peak from midday to afternoon and reach their lowest levels at night, while in other areas, they are highest in the morning or early morning and lowest in the afternoon or noon (Table S2). The increase in atmospheric PBM concentration in the early morning is possible because of the activation of regional surface emission sources during sunrise and temperature increase (Chen et al., 2013). The afternoon decline in PBM concentrations could be attributed to the photochemical redox reaction among GEM, GOM, and PBM induced by the redistribution of particles towards the gas phase (Ye et al., 2016). Moreover, anthropogenic emissions may contribute significantly to evaluated PBM concentrations during daytime activities such as agricultural and industrial production, transportation emissions, etc. (Nguyen et al., 2011). For example, motor vehicle emissions are increased during peak commuting hours, leading to higher PBM concentrations (Landis et al., 2007; Xu et al., 2015). In addition, long-range transport plays an influential role in diurnal PBM content, potentially causing the peak time of PBM concentration in remote areas to be slightly later than in other areas due to the time required for Hg transport from other areas. Photoreduction during daytime atmospheric transport may decrease PBM concentrations (Huang et al., 2019). However, the atmospheric mixing layer is much lower at night than during the day, which limits anthropogenic Hg transport and facilitates Hg dry deposition onto the vegetation canopy in remote areas, thereby reducing the nighttime atmospheric Hg concentration in remote regions (Fu et al., 2016b; Liu et al., 2019a).

3.1.3. Seasonal variations

Significant monthly variations of PBM concentrations are observed in China (Fig. 2A). Generally, PBM concentrations decrease first and then increase from January to December. The average PBM concentration in December is the highest, at 426.0 pg m^{-3}, followed by January (370.3 pg m^{-3}) and February (411.5 pg m^{-3}). The average PBM concentrations in July and August are the lowest, at 118.2 and 111.2 pg m^{-3}. Associated with the monthly changes, PBM concentrations in China exhibit distinctly seasonal variations, with the highest mean concentration observed in winter (429.3 pg m^{-3}), with the range of 26.6–1410.0 pg m^{-3} (10% ~ 90%) (Fig. 2B). In contrast, summer has the lowest mean PBM concentration of 131.6 pg m^{-3}, ranging from 8.3 to 270.0 pg m^{-3} (10% ~ 90%). The mean PBM concentrations in spring and autumn are comparable at 217.3 and 239.6 pg m^{-3}, respectively. The variations of the median PBM concentration are in line with the mean value: winter (147.8) > autumn (136.4) > spring (121.4) > summer (59.2 pg m^{-3}).

Heating can directly increase atmospheric Hg content and emit particulate matter to facilitate the adsorption of GEM or GOM, further raising atmospheric PBM concentrations (Feng et al., 2004; Xu et al., 2015; Zhang et al., 2012). Given the significant impacts of heating on PBM, the monthly variations of PBM in heating and non-heating regions in China, namely North and South China, are analyzed, respectively

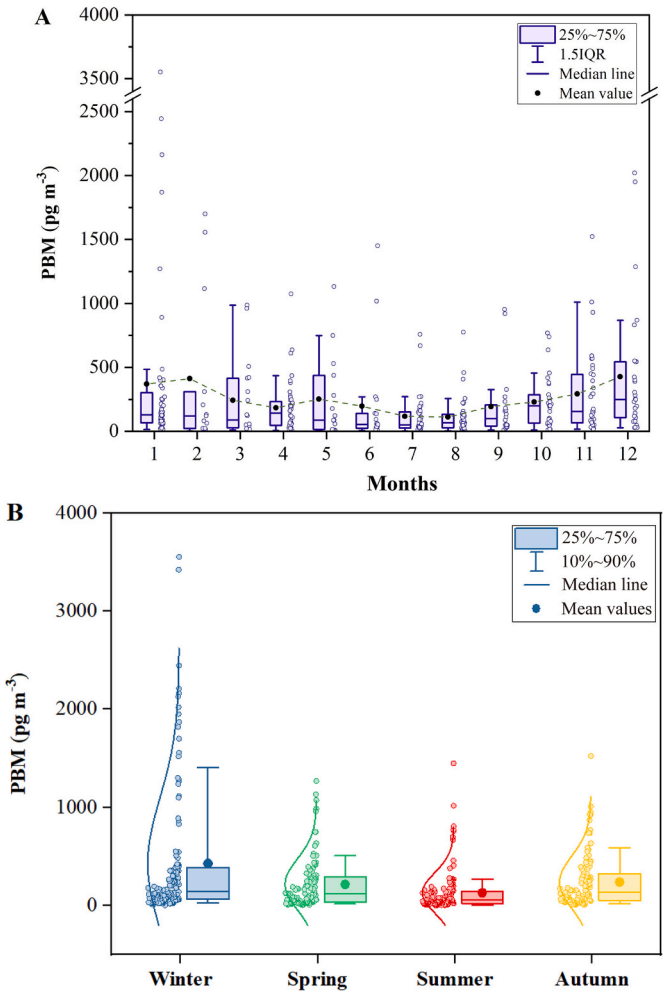

Fig. 2. Monthly (A) and seasonal (B) variations of PBM concentrations in China. The line and dot in the boxes represent the median and mean values, respectively. The bottom and top lines of the boxes are the first quartile (25%) and third quartile (75%), respectively. The upper and lower whiskers represent the data range of box diagrams. Next to the boxes are the normal fitting curves based on the data mean and standard variance, with dots representing the corresponding data. The data sources are detailed in Table S1, compiled from previous studies.

(Fig. S3). PBM concentrations in all months are higher in North China than in South China, suggesting that anthropogenic activities in North China emitted more PBM into the atmosphere. PBM concentrations are higher from November to February due to the heating in North China. South China has higher PBM concentrations from December to March, probably influenced by the Hg transport from North China. The lowest PBM concentrations are observed in July in North China and August in South China. The seasonal variations of PBM concentrations in North China and South China follow the national trend, with significantly higher mean PBM concentrations observed in North China in all seasons (Fig. S4). Overall, although some studies have reported the highest PBM concentration in spring (Zhang et al., 2019) or autumn (Sun et al., 2021), the general trend for PBM concentration in China is winter > autumn ≈ spring > summer (Qin et al., 2016; Qin et al., 2019; Wang et al., 2021a; Xu et al., 2020; Yuan et al., 2021).

The similar seasonal variations in PBM in northern and southern China suggest that other factors besides heating influence PBM variation in China. Meteorological factors, such as air temperature, relative humidity, aerosol compositions, mixing layer height, rainfall, and desert dust, probably contribute to the PBM variations. Atmospheric temperature and relative humidity can impact the variation of PBM content by

affecting the gas-particle distribution of Hg (Qin et al., 2016; Wang et al., 2020; Xu et al., 2015). The higher temperature in summer increases atmospheric Hg distribution to the gas phase (Rutter and Schauer, 2007), while the lower temperature in winter raises the transformation from GEM and GOM to PBM (Liu et al., 2022a; Selin et al., 2007). The high relative humidity occurring in cold seasons contributes to the oxidation of GEM into GOM through OH radicals (Holmes et al., 2009) and the formation of an aqueous phase layer near insoluble mineral particles (Sun et al., 2013b), which increases its volume to dissolve and adsorb more GOM (Zhang et al., 2019). In China, November to April is considered cold, while May to October is warm. Previous studies have indicated that the PBM content is typically higher in the cold months compared to the warm months (Duan et al., 2017b; Hong et al., 2016a; Hong et al., 2016b; Qin et al., 2019; Schleicher et al., 2015; Zhang et al., 2021a). Low atmospheric temperature and high relative humidity during the cold months contribute to enhanced atmospheric gas-particle partitioning, leading to the transformation of atmospheric GEM to GOM and PBM in China (Fain et al., 2009; Lin et al., 2019; Xu et al., 2020). In addition to temperature and relative humidity, aerosol compositions also significantly impact the gas-particle distribution of atmospheric Hg. GOM tends to be adsorbed on particles containing organics, NO_3^-, and chloride, whereas when particles contain more SO_4^{2-} and NH_4^+, GOM tends to exist in the gas phase (Xu et al., 2020). The lower mixing layer height in cold seasons is not facilitative to the diffusion of atmospheric particles, providing more adsorption medium for Hg and resulting in PBM accumulation (Hong et al., 2016b; Qin et al., 2019; Schleicher et al., 2015). For instance, the shallower boundary layer resulted in the highest PBM content in urban Hefei in January, and the elevated PBM concentrations in the morning and evening were also related to the lower boundary layer depth (Hong et al., 2016a). Additionally, in China, summer has the highest rainfall and consequently facilitates the rapid removal of atmospheric PBM through wet deposition (Schleicher et al., 2015; Wang et al., 2020; Zhang et al., 2019).

Atmospheric transports also contribute significantly to seasonal PBM variations. (Wang et al., 2021a; Zhang et al., 2015). In eastern China, winter and spring seasons are mainly affected by the north and west winds, which increases the regional PBM concentrations (Duan et al., 2017a; Yuan et al., 2021). In summer, east and south winds from the sea with low pollution concentrations primarily influence PBM concentrations (Duan et al., 2017a; Qin et al., 2023). For instance, elevated levels of PBM in Waliguan mountain were observed during the cold months due to the strengthening of the westerly winds from anthropogenic emission regions or those passing through such regions (Zhang et al., 2015). Additionally, desert dust has an enhanced effect on the transport of atmospheric PBM (Zhang et al., 2021a). Winter and spring sandstorms in northwest China and other regions may provide a critical carrier for atmosphere Hg adsorption (Zhang et al., 2021a; Zhang et al., 2019). Nie et al. (2020) speculated that the transport of Hg adsorbed on desert dust with strong winds during desert dust events may have decreased local PBM concentrations but exacerbated the PBM concentrations in the dust transport regions (Nie et al., 2020).

Heating during winter releases more Hg into the atmosphere, and the emitted particulate matter by human activities also provides more surfaces for the adsorption of other Hg species, resulting in an increase in PBM concentration (Duan et al., 2016; Feng et al., 2004; Xu et al., 2015). Moreover, mid-November to mid-March is the heating period in northern China (He et al., 2001), with the lowest temperature throughout the year. Thus, December, January, and February present the highest PBM concentrations of the year. Due to the high atmospheric temperature and rainfall in warm months, PBM is easily soluble in water and can be rapidly removed by wet deposition (Blanchard et al., 2002; Cole et al., 2014). Especially in July and August in China, the lowest PBM concentrations occur due to favorable meteorological conditions for atmospheric Hg diffusion and no increase in anthropogenic Hg emissions such as heating.

3.1.4. Long-term trends

To determine the annual trend of PBM in China, we performed seasonal differentiation on the data of published articles, as some studies did not monitor the PBM concentration throughout the year during their study periods, and the PBM concentrations in different seasons vary significantly (Fig. 3, Fig. S5). In general, the PBM concentration in China exhibited an increasing trend, followed by a subsequent decrease from 1999 to 2018, reaching its peak concentration in 2013 (Fig. 3, Fig. S5). According to emission inventory results, Zhang et al. (2023) found that anthropogenic Hg emissions in China from 1980 to 2020 had a similar trend and divided it into three stages: the fast development stage driven by economic factors, the growth control offset stage, and the rapid decline period of economic decoupling. Many studies were carried out during 2010–2015, which is the period with the highest PBM concentrations in China (Table S1, Fig. S5), attributed to the high Hg emissions from coal-fired power plants, coal-fired boilers, and small-scale artisanal gold production (Wu et al., 2016). The four seasons, including spring, summer, autumn, and winter, also have the highest PBM concentrations during this period (Fig. 3). Atmospheric PBM concentrations began to decline after 2013, with a significant drop occurring since 2015. The consecutive decline in atmospheric Hg emissions after 2013 was attributed to air pollution control measures implemented in industries, such as the improvement of dedusting, desulfurization, and denitrification devices (Liu et al., 2019c). Currently, cement production has surpassed power plants and industrial boilers to become the largest source of Hg emissions (Liu et al., 2019c; Zhang et al., 2023). The high PBM concentrations in China mostly occur in urban areas, such as Beijing, Shanghai, Nanjing, Chengdu, etc., suggesting extreme impacts of anthropogenic emissions (Chen et al., 2016; Wang et al., 2006; Xu et al., 2017; Xu et al., 2019; Zhu et al., 2014). Schleicher et al. (2016) demonstrated that the observed PBM content in Beijing increased first and then decreased from 2005 to 2013. The measures implemented during the Olympic Games, such as reducing traffic, increasing public transportation, increasing green space, and prohibiting industrial activities, led to the lowest PBM concentration in the summer of 2008 (Schleicher et al., 2016).Meanwhile, decreased GEM concentrations are also found in China. Fu et al. (2015) observed that the GEM concentration in Changbai Mountain, a remote region of China, exhibited an increase from 2009 to 2013, followed by a decrease from 2013 to 2015. Similarly, Tang et al. (2018) observed a notable decrease in GEM concentrations in rural eastern China from 2014 to 2016.

Declines in atmospheric Hg concentrations had been observed earlier in other parts of the world than in China (Cole et al., 2013; Slemr et al., 2011; Weigelt et al., 2015; Weiss-Penzias et al., 2016; Zhang et al., 2016). Weiss-Penzias et al. (2016) showed that from 1997 to 2013, about half of the observation sites in the United States and Canada exhibited a decline in atmospheric Hg wet deposition, while the remaining observation points did not observe a significant increasing trend. The observation results by Slemr et al. (2011) in the Southern Hemisphere and the Atlantic Ocean indicated a decrease in atmospheric Hg content by approximately 20% - 38% from 1996 to 2009, contradicting the almost constant anthropogenic emissions estimated by the Hg emission inventory. They believed that climate change, ocean acidification, and the reduction of re-emission of historical Hg were the main reasons for this result, especially the latter. Similarly, Zhang et al. (2016) also pointed out that the observed atmospheric GEM concentration decreased by about 1–2% per year from 1990 to 2010. They speculate that the Hg emission inventory method could not adequately account for reductions in Hg emissions from commercial and coal-burning activities, nor did it accurately estimate Hg emissions from artisanal and small-scale gold mining, leading to overstated results. In addition, Hg emissions in Asia increased during this period compared to decreases in North America and Europe (Zhang et al., 2016).

3.1.5. Factors influencing PBM emissions

The environmental factors, including air quality index and

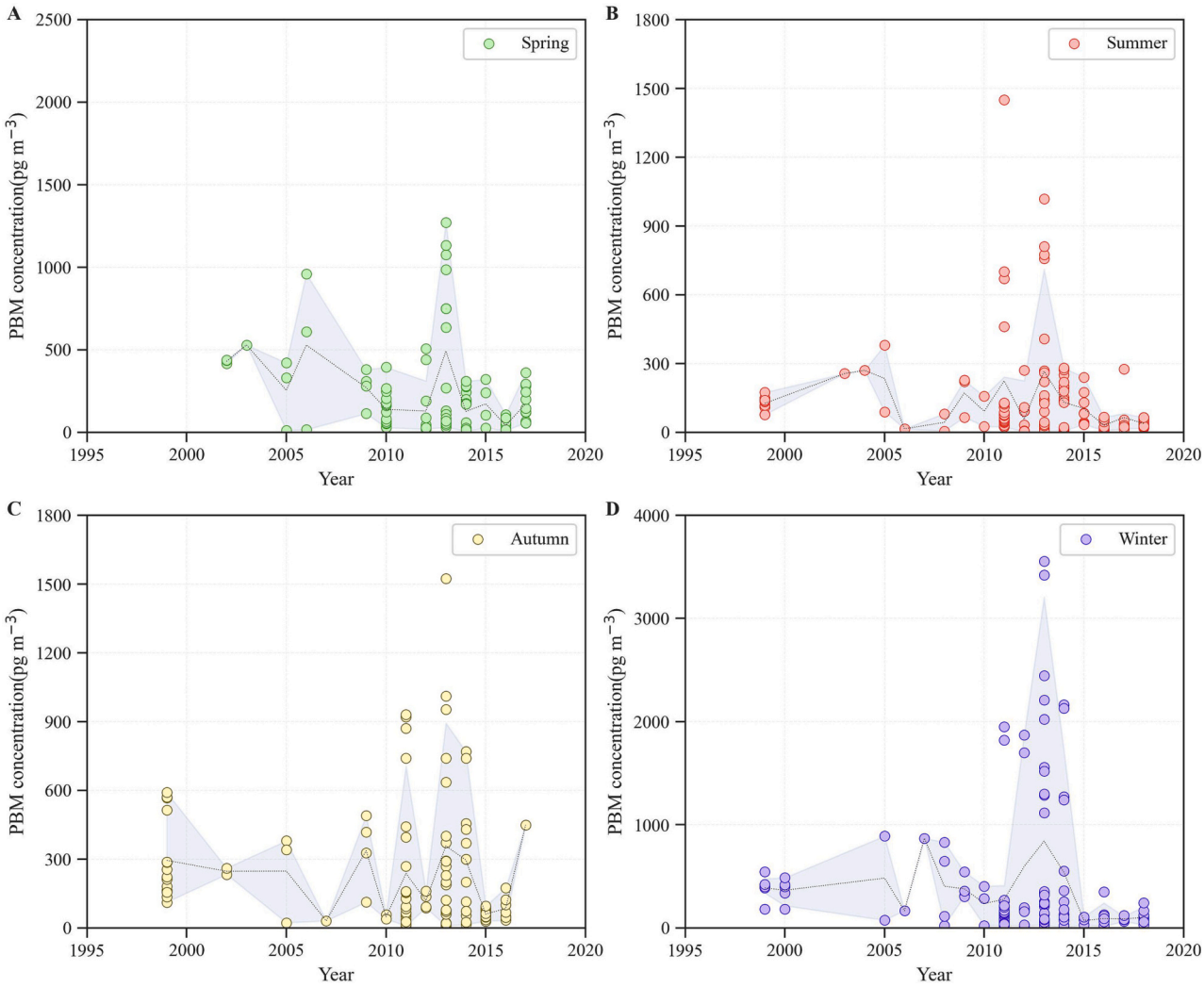

Fig. 3. Annual variations of PBM concentrations in spring (A), summer (B), autumn (C), and winter (D) in China. The data are derived from previous studies, as described in Table S1. The shaded area's upper and lower bounds represent Q3 + 1.5IQR and Q1–1.5IQR of the data, respectively, and the dashed line represents the mean values.

meteorological conditions, were obtained from a previous study (Tang et al., 2021) to understand better the contributions affecting atmospheric PBM contents. PCA results revealed three factors that explained 77.6% of the total variance (Table S3). Factors F1 can be labeled as the anthropogenic source, accounting for 44.5%, and factors F2 and F3 can be classified as the natural source (atmospheric transport and process), accounting for 23.8% and 9.26%, respectively (Text S2, Table S3). Moreover, based on the MLR result, local anthropogenic sources, atmospheric transport, and local atmospheric transformation contributed 56.2%, 14.9%, and 29.0% to the content over China, respectively (Table S3). In contrast to the positive contribution of anthropogenic emissions to PBM levels, the negative regression coefficients of the MLR model suggest the negative impact of atmospheric transport and transformation on PBM content. Atmospheric transports can dilute atmospheric Hg concentrations, primarily in areas with high PBM content (Qin et al., 2023). However, it should be noted that it may be the dominant PBM source in areas with low Hg concentrations, such as remote or rural areas (Fu et al., 2019a; Mao et al., 2016). Also, atmospheric processes like photoredox reactions can change PBM concentrations (Liu et al., 2022a; Zheng et al., 2021). For example, Zhang et al. (2022) estimated that about 21% to 46% of PBM was converted to Hg(0) by photoreduction and then released into the atmosphere.

3.2. *Stable isotopes revealing Hg circulation*

3.2.1. *Hg isotopes compositions of natural materials*

We summarized the Hg isotopic fractionation of general Hg-containing materials, as shown in Fig. 4 and Fig. S6. The literature pertaining to Hg isotopes in the following figures is sourced from the references listed in Fig. 4. The Hg isotope fractionation of natural materials in the environment is significant, ranging from −4.37‰ to 4.07‰ for δ^{202}Hg (n = 4316), from −5.08‰ to 7.59‰ for Δ^{199}Hg (n = 4281), and from −0.26‰ to1.19‰ for Δ^{200}Hg (n = 3443) (Fig. 4). The medians of δ^{202}H, Δ^{199}Hg, and Δ^{200}Hg for the natural materials are −0.67‰, and − 0.02‰, and 0.02‰, respectively.

The Hg isotope ratios in air Hg samples widely range from −3.69‰ to 3.36‰ for δ^{202}Hg and from −2.34‰ to 1.50‰ for Δ^{199}Hg (Fig. 4, Table S4). Specifically, significant negative mean (± 2SD) values for δ^{202}Hg are observed for PBM (−0.83‰ ± 1.21‰) and GEM/TGM (−0.25‰ ± 1.30‰), the mean (± 2SD) δ^{202}Hg value of Arctic PBM is near zero (−0.06‰ ± 1.61‰), while the majority of Antarctic PBM and Arctic GEM have positive values for δ^{202}Hg. PBM exhibits a slightly positive mean (± 2SD) value for Δ^{199}Hg (0.08‰ ± 0.75‰), while GEM/TGM has a slightly negative mean (± 2SD) value for Δ^{199}Hg (−0.08‰ ± 0.18‰). Additionally, PBM displays a broad range of Δ^{199}Hg fractionation (−1.39‰ ~ 1.50‰) in contrast to GEM (−0.27‰ ~ 0.19‰). Most

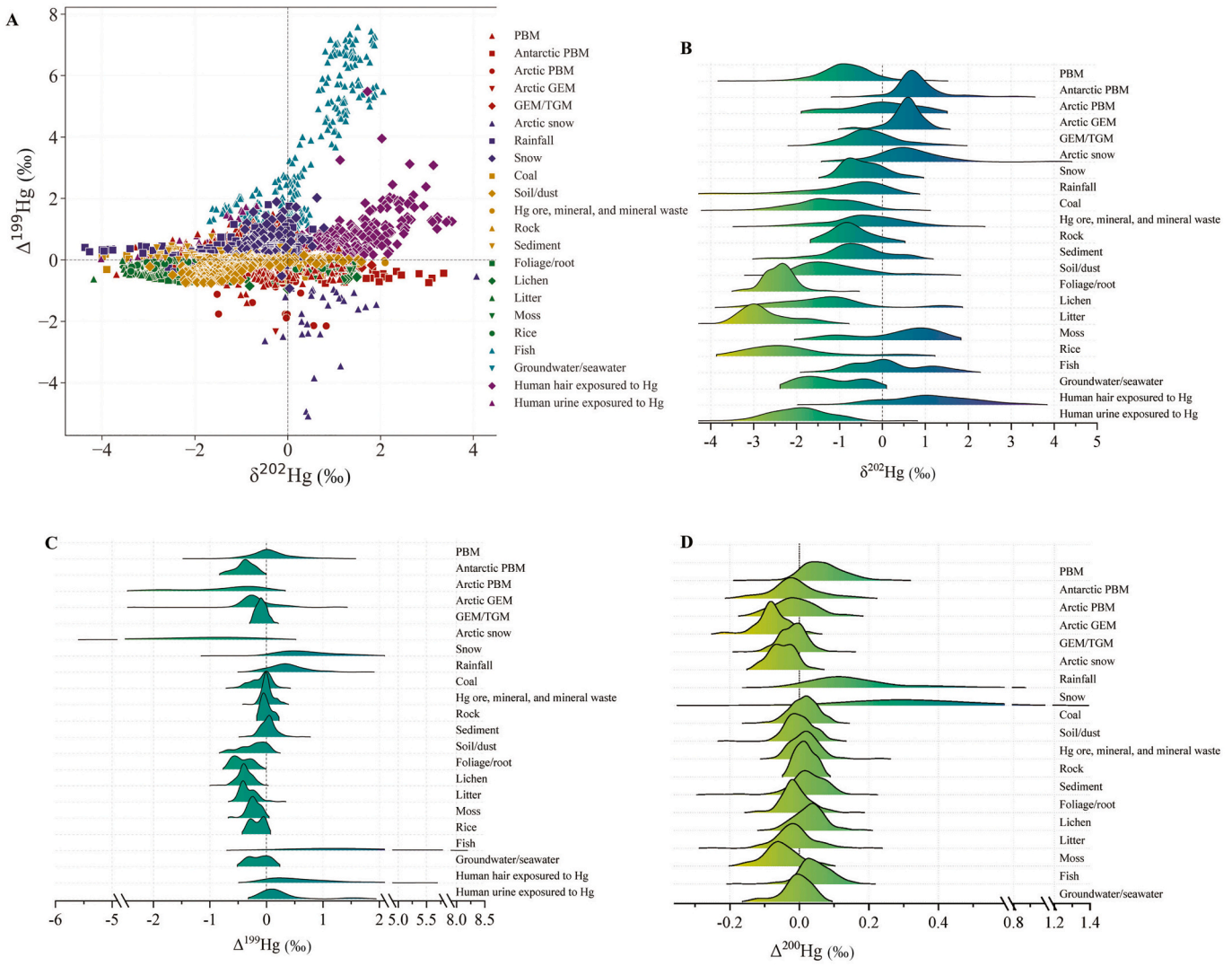

Fig. 4. $\delta^{202}Hg$ versus $\Delta^{199}Hg$ (A) and kernel density estimations for $\delta^{202}Hg$ (B), $\Delta^{199}Hg$ (C), and $\Delta^{200}Hg$ (D) of natural materials in the environment. The natural materials include PBM (except for the polar regions) (Fu et al., 2019a; Huang et al., 2016; Huang et al., 2019; Huang et al., 2020b; Liu et al., 2022a; Qin et al., 2023; Qiu et al., 2021; Sun et al., 2021; Xu et al., 2017; Xu et al., 2019; Xu et al., 2021; Yu et al., 2016; Zhang et al., 2022), Antarctic PBM (Li et al., 2020), Arctic PBM (Araujo et al., 2022; Zheng et al., 2021), Arctic GEM (Araujo et al., 2022; Sherman et al., 2010; Zheng et al., 2021), GEM/TGM (except for the polar regions) (Demers et al., 2013; Fu et al., 2016a; Fu et al., 2021b; Gratz et al., 2010; Yu et al., 2016; Yu et al., 2022; Zheng et al., 2021), Arctic snow (Araujo et al., 2022; Sherman et al., 2010; Zheng et al., 2021), rainfall (Demers et al., 2013; Gratz et al., 2010; Sherman et al., 2012; Wang et al., 2015; Xia et al., 2022; Yuan et al., 2022a), snow (Wang et al., 2015; Yuan et al., 2022a), coal (Biswas et al., 2008; Huang et al., 2016; Huang et al., 2017; Lefticariu et al., 2011; Sherman et al., 2012; Sun et al., 2014a; Sun et al., 2013a; Sun et al., 2014b; Tang et al., 2017; Wang et al., 2015; Yin et al., 2014a), soil/dust (Biswas et al., 2008; Demers et al., 2013; Estrade et al., 2011; Huang et al., 2016; Jiskra et al., 2017; Lepak et al., 2022; Liu et al., 2019b; Wang et al., 2017; Wang et al., 2015; Xia et al., 2022; Yin et al., 2013b; Yuan et al., 2022b; Zheng et al., 2016), Hg ore, mineral, and mineral waste (Cooke et al., 2013; Jiskra et al., 2017; Lefticariu et al., 2011; Sonke et al., 2010; Stetson et al., 2009; Wang et al., 2015; Wiederhold et al., 2013; Yin et al., 2013c), rock (Huang et al., 2016; Sun et al., 2014a; Wang et al., 2015; Xia et al., 2022; Yuan et al., 2022b), sediment (Cooke et al., 2013; Donovan et al., 2013; Foucher and Hintelmann, 2009; Gantner et al., 2009; Gehrke et al., 2011a; Lepak et al., 2015; Mil-Homens et al., 2013; Sonke et al., 2010; Sun et al., 2022; Yin et al., 2015; Yin et al., 2013c), foliage/root (Demers et al., 2013; Liu et al., 2019b; Yuan et al., 2022b; Zheng et al., 2016), lichen (Božič et al., 2022; Carignan et al., 2009; Estrade et al., 2010), litter (Jiskra et al., 2015; Wang et al., 2017; Yu et al., 2016; Zheng et al., 2016), moss (Jiskra et al., 2019; Liu et al., 2019b), rice (Yin et al., 2013a), fish (Gantner et al., 2009; Gehrke et al., 2011b; Laffont et al., 2009; Lepak et al., 2022; Tsui et al., 2014; Yang et al., 2022), groundwater/seawater (Huang et al., 2017; Jiskra et al., 2017; Xia et al., 2022), human hair exposed to Hg (Du et al., 2018; Laffont et al., 2009; Li et al., 2014; Li et al., 2016; Li et al., 2017; Rothenberg et al., 2017; Sherman et al., 2015; Sherman et al., 2013; Yang et al., 2021), and human urine exposed to Hg (Du et al., 2021; Sherman et al., 2015; Sherman et al., 2013).

air Hg samples have negative values for $\Delta^{199}Hg$ in the polar regions, especially for Arctic PBM and Arctic GEM, whose minimum values of $\Delta^{199}Hg$ are less than −2.00‰. Zheng et al. (2021) pointed out that the negative $\triangle^{199}Hg$ of PBM in the Arctic was mainly derived from the in-situ oxidation of GEM and subsequent particle scavenging rather than directly from the long-distance transport of PBM from anthropogenic emissions. Additionally, PBM exhibits a positive mean (± 2SD) $\Delta^{200}Hg$ value of 0.07‰ ± 0.12‰ (Table S4), surpassing that of other atmospheric samples, including Antarctic PBM (−0.01‰ ± 0.13‰), Arctic PBM (−0.01‰ ± 0.11‰), Arctic GEM (−0.08‰ ± 0.09‰), and GEM/TGM (−0.02‰ ± 0.08‰). The positive $\Delta^{200}Hg$ of PBM may be attributed to photochemical redox reactions occurring in aerosols within the troposphere (Cai and Chen, 2016; Fu et al., 2021a). Significantly positive $\delta^{202}Hg$, negative $\Delta^{199}Hg$, and negative $\Delta^{200}Hg$ values are observed in Arctic snow samples, ranging from −1.06‰ to 4.07‰, −5.08‰ to 0.01‰, and − 0.12 to 0.04 respectively (Fig. 4). The negative

MIF in Arctic snow possibly originates from the photoreduction of Hg (II) (Sherman et al., 2010), and Arctic warming probably accelerates the deposition of atmospheric Hg (II) to snow (Steffen et al., 2014). However, most snow and rainfall samples in other regions have significantly negative δ^{202}Hg, positive Δ^{199}Hg, and Δ^{200}Hg values.

Generally, solid natural materials exhibit negative mean (± 2SD) values of δ^{202}Hg, which are −1.28‰ ± 1.61‰ for coals, −1.10‰ ± 1.62‰ for soils/dust, −0.38‰ ± 1.80‰ for Hg ores, minerals, and mineral waste, −0.73‰ ± 0.93‰ for rocks, and − 0.64‰ ± 1.45‰ for sediments (Table S4). As shown in Fig. 4, the values of δ^{202}Hg of PBM and GEM/TGM mostly overlap with those of solid natural materials. The mean (± 2SD) Δ^{199}Hg values of solid natural materials are near-zero or slightly negative, such as coals (−0.09‰ ± 0.37‰), Hg ores, minerals, and mineral waste (0.02‰ ± 0.21‰), rocks (−0.00‰ ± 0.18‰), sediments (0.04‰ ± 0.29‰), and soils/dust (−0.23‰ ± 0.46‰). For vegetations, foliage/roots (−2.39‰ ± 0.74‰) and litters (−2.69‰ ± 1.22‰) have negative δ^{202}Hg values, while lichens (−1.32‰ ± 2.21‰), mosses (0.32‰ ± 1.85‰,), and rice (−2.06‰ ± 2.19‰) have a broader range of δ^{202}Hg values. Most of the Δ^{199}Hg values are negative for all of them, with the mean (± 2SD) values of −0.42‰ ± 0.34‰ for foliage/roots, −0.32‰ ± 0.29‰ for litters, −0.38‰ ± 0.28‰ for lichens, −0.22‰ ± 0.24‰ for mosses, −0.16‰ ± 0.25‰ for rice.

Fish and human hair exposed to Hg have similar patterns of δ^{202}Hg and Δ^{199}Hg (Fig. 4, Table S4). The mean (± 2SD) values of δ^{202}Hg of fish and human hair are 0.15‰ ± 1.65‰ and 1.10‰ ± 2.02‰, and their mean (± 2SD) values of Δ^{199}Hg are 2.55‰ ± 4.39‰ and 0.67‰ ± 1.46‰, which are remarkably higher than the Δ^{199}Hg values of solid materials and vegetations. The mean (± 2SD) values of δ^{202}Hg Hg of groundwater/seawater and human urine exposed to Hg are −1.21‰ ± 1.33‰ and − 1.92‰ ± 1.44‰, respectively, and the mean (± 2SD) values of Δ^{199}Hg of them are −0.13‰ ± 36‰ and 0.28‰ ± 0.93‰, respectively. Fish and rice grown in heavily Hg-polluted regions serve as a significant source of human Hg intake. The Δ^{199}Hg in human hair and urine, primarily obtained through fish consumption, exhibit markedly positive values, whereas those derived from rice consumption are near zero (Du et al., 2018; Rothenberg et al., 2017). Furthermore, lighter Hg isotopes are preferentially involved in the demethylation process of MeHg within the human body, resulting in lower δ^{202}Hg values in urine and higher δ^{202}Hg values in hair (Li et al., 2022). In contrast, the fractionation of ingested Δ^{199}Hg in the human body is relatively minor (Li et al., 2022).

3.2.2. *Hg flows revealed by SEM*

Polar regions exhibit higher δ^{202}Hg values of GEM and PBM than other regions, especially the δ^{202}Hg values of Arctic GEM and Antarctic PBM are significantly positive (Fig. 4). Moreover, the Δ^{199}Hg values of GEM and PBM in polar regions are mainly negative, similar to the δ^{202}Hg and Δ^{199}Hg ratios of polar snow. In the Arctic, PBM mostly stems from in-situ oxidation of GEM and following particle scavenging, thereby inheriting the isotopic ratio of GEM (Zheng et al., 2021). Additionally, studies have shown that during atmospheric Hg depletion events, large amounts of Hg in the snow are re-released into the atmosphere through photochemical processes in polar regions, leading to elevated atmospheric Hg concentrations (Steffen et al., 2015; Wang et al., 2019). In contrast, other areas show negative δ^{202}Hg values and significantly positive Δ^{199}Hg values in rainfall and snow samples. The positively shifted Δ^{199}Hg is likely affected by atmospheric photoredox processes, which is supported by the high Δ^{200}Hg values of rainfall (0.16‰ ± 0.26‰) and snow (0.38‰ ± 0.50‰) associated with strong photo-initiated oxidation (Chen et al., 2012) (Fig. S6).

Most atmospheric Hg samples (GEM/TGM, PBM, rainfall, and snow) have negative δ^{202}Hg values, primarily overlapped with the values of solid natural materials (coals, Hg ores, minerals, and mineral waste, rocks, sediments, and soils/dust) and vegetations (foliage/roots, litters, lichens, mosses) (Fig. 4). However, due to the significant influence of atmospheric transport, GEM generally shows a distinctively positive δ^{202}Hg and negative Δ^{199}Hg in remote regions (Fu et al., 2019b; Yu et al., 2022), while other Hg(II) compounds are typically characterized by positive Δ^{199}Hg (Qin et al., 2023; Yuan et al., 2022a). The comparable isotopic variations between atmospheric Hg samples and solid natural materials imply a significant contribution of solid natural materials and vegetation to atmospheric Hg, as substantial MIF is solely triggered by intensive photooxidation and photoreduction (Blum et al., 2014; Cai and Chen, 2016). The results of the SEM (Fig. 5) demonstrate the conclusion with the extreme relationship ($P < 0.01$) between atmospheric Hg and raw materials (estimate coefficient = 0.91) and vegetation (estimate coefficient = 1.78). Although MDF of Hg occurs during coal combustion, it is typically around 0.3‰, and no MIF was observed in this process (Sun et al., 2013a). Therefore, it is practical to trace Hg emissions from coal combustion using Hg isotopes. Compared with Hg emissions from raw materials, the relationship between plant and atmospheric Hg has a higher estimate coefficient, which may be because plants are not only a source of Hg emissions but also a pool for Hg absorption. Previous studies have shown that biomass burning is one of the important sources of atmospheric Hg, and it would not change the Δ^{199}Hg values during combustion (Han et al., 2023; Huang et al., 2016). But at the same time, vegetation is also an import absorption and storage pool of atmospheric Hg and a main source of raw coal (Hatcher and Clifford, 1997; Wang et al., 2021c). Atmospheric Hg can be deposited in terrestrial and marine ecosystems through wet and dry deposition (Howard and Edwards, 2018; Sprovieri et al., 2017; Yang et al., 2010). However, historically deposited Hg can also increase atmospheric Hg levels through re-emission (AMAP/UNEP, 2013; AMAP/UNEP, 2019). In addition to the significant impact of atmospheric Hg deposition on vegetation, soil/dust is also significantly ($P < 0.01$, Fig. 5) related to Hg accumulation in plants, as plant roots can uptake Hg from soils (Yuan et al., 2022b). For instance, Hg in the roots of subtropical forest comes mainly from the surrounding soil, and in karstic forest areas, about 80% of the Hg in the soils originates from litterfall Hg depositions (Yuan et al., 2022b; Du et al., 2023).

Due to the limited number of urine and water samples, we combined urine with hair samples and water with fish samples for SEM analysis (Fig. 5). We found that atmospheric Hg, as well as Hg in water and fish, have significant ($P < 0.01$) effects on the human body. Previous studies have emphasized the significant transfer of Hg from fish to humans (Sunderland, 2007), as evidenced by the comparable Hg isotope ratios observed in fish and human hair (Fig. 4). The Hg isotopic compositions in human urine also closely resemble those in rice and groundwater, suggesting their potential significance as sources of human Hg intake (Du et al., 2018; Xia et al., 2022). Moreover, the human body has a higher regression coefficient with atmospheric Hg than water and fish, indicating that the human body's inhalation of atmospheric Hg cannot be ignored. In addition, atmospheric Hg deposition significantly impacts ($P < 0.01$) the Hg isotope compositions of water and fish, and the deposited Hg then accumulates in sediments through sedimentation (Fig. 5).

3.2.3. *PBM sources identified by Hg isotopes*

3.2.3.1. PBM isotope ratios in China. As shown in Fig. 6 and Fig. S7, the observed PBM isotopic compositions in China range from −3.69‰ to 1.19‰ for δ^{202}Hg (−0.83‰ ± 1.21‰, mean ± 2SD, $n = 859$), −1.39‰ to 1.50‰ for Δ^{199}Hg (0.08‰ ± 0.75‰, mean ± 2SD, n = 859), and − 0.16‰ to 0.29‰ for Δ^{200}Hg (0.07‰ ± 0.12‰, mean ± 2SD, $n = 814$). Most of the δ^{202}Hg values of PBM in China are negative, which overlap with most of the Hg emissions sources, such as coals, soils/dust, and moss (Fig. 6, Fig. S8). The highest Δ^{199}Hg value of PBM is found in remote/rural areas (0.40‰ ± 0.73‰, mean ± 2SD, $n = 122$), followed by islands (0.35‰ ± 0.67‰, mean ± 2SD, $n = 21$), suburban (0.10‰ ± 0.32‰, mean ± 2SD, $n = 20$), urban (0.10‰ ± 0.71‰, mean ± 2SD, $n = 481$), and coastal areas (−0.17‰ ± 0.52‰, mean ± 2SD, $n = 215$).

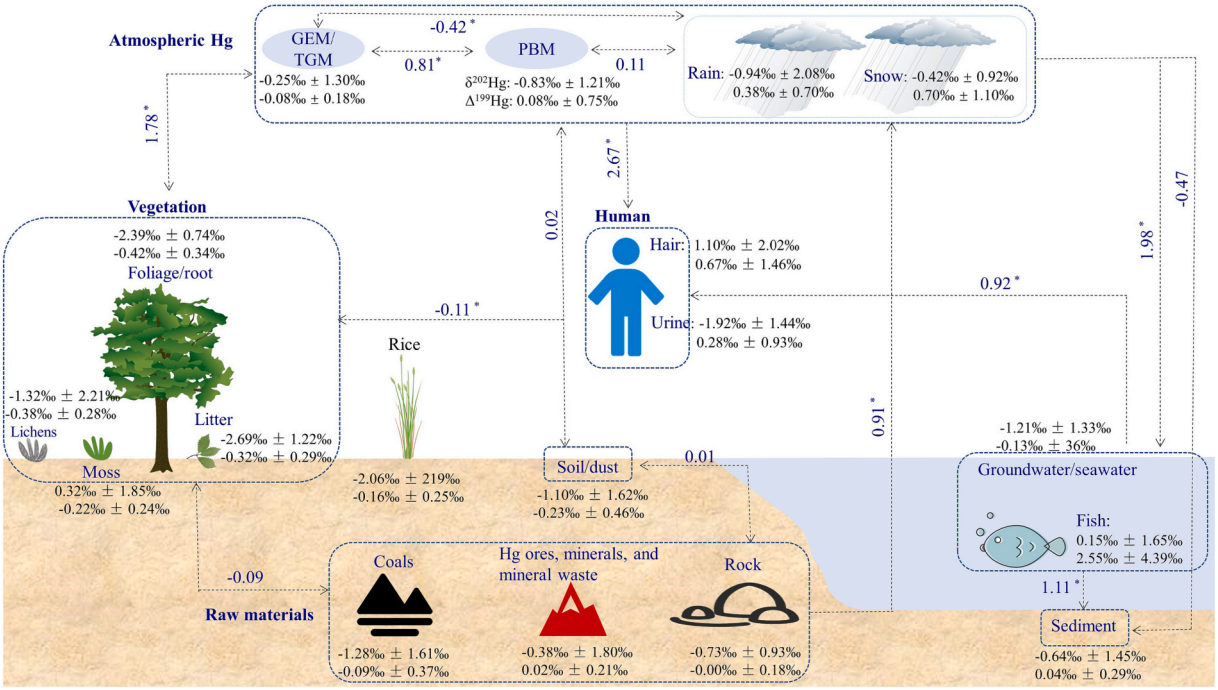

Fig. 5. Hg circulation in the environment illustrated by Hg isotopes (δ^{202}Hg and δ^{199}Hg) and the structural equation modeling (SEM). The first and second lines of text near each natural material are its δ^{202}Hg and Δ^{199}Hg (mean ± 2SD) values, respectively. Due to the limited sample data, the impact of rice on human Hg was excluded when constructing the SEM. The *P* value of the SEM is <0.001, and the comparative fit index is 0.86. * Indicates an extremely significant relationship ($P < 0.01$) between elements. The dataset is the same as in Fig. 4, excluding those from polar regions.

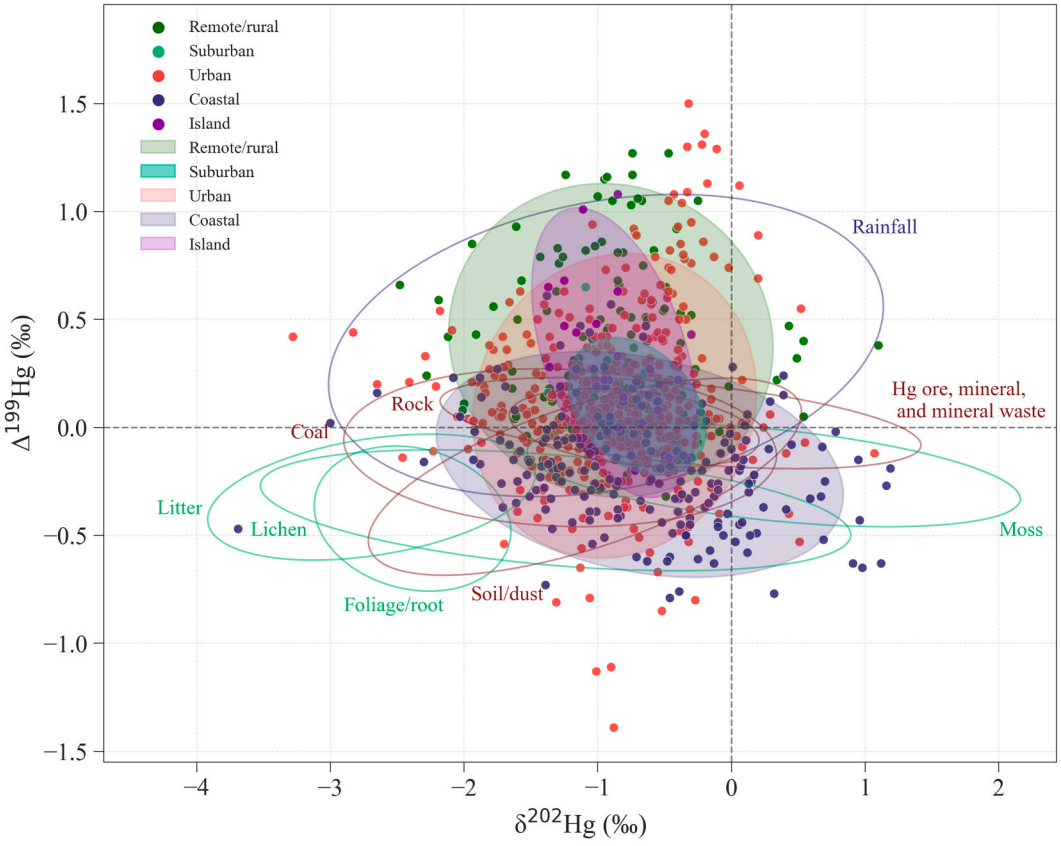

Fig. 6. Hg isotope ratios (δ^{202}Hg versus Δ^{199}Hg) of PBM in China (Fu et al., 2019b; Huang et al., 2016; Huang et al., 2019; Huang et al., 2020b; Liu et al., 2022a; Qin et al., 2023; Qiu et al., 2021; Sun et al., 2021; Xu et al., 2017; Xu et al., 2019; Xu et al., 2021; Yu et al., 2016; Zhang et al., 2022). The labeled categories - Remote/rural, Suburban, Urban, Coastal, and Island - represent corresponding PBM samples. The ellipses illustrate the 95% confidence level calculated from the variance-covariance matrix of Hg isotope values in each material. The references involved in the dataset of Hg sources are listed in Fig. 4.

Given the δ^{202}Hg and Δ^{199}Hg values of PBM and Hg emissions sources, PBM in urban and suburban is mainly from industrial activities, such as coal combustion and metal smelting, followed by biomass burning (moss and lichens). Moreover, biomass burning is a significant contributor in coastal areas compared to other regions. However, some Δ^{199}Hg values of PBM in China, like remote and island areas, are significantly positive instead of near-zero or negative values, indicating that factors other than human activities also contribute significantly to PBM levels. Previous studies have pointed out that Hg undergoes strong photoreduction during long-distance transports, resulting in a positive shift in Δ^{199}Hg values (Chen et al., 2012; Fu et al., 2019a; Qiu et al., 2021), which suggests that not only GEM but also PBM can carry out long-distance transport in the atmosphere. Similar positive Δ^{199}Hg values also appear in rainfall samples. Fig. S9 illustrates the correlation between Δ^{199}Hg and Δ^{201}Hg, and the slope is widely used to identify Hg MIF processes. For instance, the slope is approximately 1.36 in residual MeHg following photodegradation, and the ratio in freshwater fish is 1.28 (Blum et al., 2014). The Δ^{199}Hg /Δ^{201}Hg ratio of PBM samples in China is 1.11 ± 0.02 (2SE, n = 841, Fig. S9), close to the slopes in the residual phase of Hg(II) photoreduction (1.00–1.31) (Bergquist and Blum, 2007; Zheng and Hintelmann, 2009), indicating that atmospheric Hg photoreduction is the primary reaction experienced by PBM in China.

According to the linearized binary isotope mixing equation, δ^{202}Hg versus 1/PBM and Δ^{199}Hg versus 1/PBM are used to estimate the Hg isotope compositions of PBM from anthropogenic and background atmospheric sources in China (Fig. S10). Assuming that when 1/PBM is zero, all PBM in aerosols come from anthropogenic sources, i.e., the contribution of atmospheric background sources is zero (Fu et al., 2018). At this point, the estimated δ^{202}Hg and Δ^{199}Hg values of anthropogenic sources contributing to PBM in China are −0.79‰ and 0.02%, respectively, closely resembling the values of the abovementioned anthropogenic sources (coals, rock, etc.). Regionally, most δ^{202}Hg and Δ^{199}Hg values of PBM in urban, suburban, and coastal areas are close to the estimated values of anthropogenic emissions, suggesting that anthropogenic sources are the most significant contributors to PBM in these regions. Nevertheless, background sources, as well as anthropogenic sources, contribute significantly to PBM levels in remote/rural and island areas. The background sources may originate from the long-distance transport of Hg, leading to a positive shift of Δ^{199}Hg of PBM (Fu et al., 2019a; Qin et al., 2023).

3.2.3.2. PBM sources prediction by machine learning

3.2.3.2.1. Isotopic tracing principles. The difficulties in isotope tracing arise from the variety of emission sources, overlap in isotope values from different sources, and isotope fractionation during emission (such as combustion) and post-emission (like transport) processes. These challenges are common to all isotope tracing models currently available in the literature. Previous studies have indicated that the number of employed emission sources significantly influences the contributions of each source when using the MixSIAR model (Luo et al., 2022). Altering the types of emission sources leads to notable changes in the estimated contributions from other sources (Feng et al., 2023). However, it is challenging to determine which sources significantly contribute to sinks and how to differentiate their effects. Additionally, atmospheric pollution is highly influenced by atmospheric transport, leading to diverse pollution sources (Qin et al., 2023; Yu et al., 2022). In this study, we selected the most common and contributing pollution sources, including industrial sources (coal, minerals, rock), biomass sources (foliage/roots, litters, lichens, mosses), and soil/dust (Huang et al., 2020a; Sun et al., 2021; Xu et al., 2021). Different regions, such as remote/rural, suburban, urban, and coastal areas, are primarily impacted by these three source categories, although their contributions to PBM vary significantly across different regions (Qin et al., 2023).

RFM operates differently from traditional methods, like MixSIAR, complementing each other. Traditional models employ regression to determine source contributions, while machine learning algorithms, such as RFC, use classification models to estimate the probabilities of PBM originating from different sources (Moore and Semmens, 2008; Pedregosa et al., 2011). Initially, the datasets of source samples are divided into training and testing sets. During training, the RFC model learns to associate different isotope compositions with specific source categories using the training set. Subsequently, the trained model predicts and classifies the testing set, evaluating its accuracy. If the accuracy falls short, the model is adjusted iteratively to maximize accuracy or meet the required predictive accuracy. Once trained, the model uses the isotope signatures of PBM to identify the probabilities of its origin from different sources. As for the overlap between different sources, the accuracy obtained on the testing set reflects the model's ability to differentiate and identify source types, a feature lacking in traditional source apportionment models. Additionally, the MixSIAR model typically uses the mean and standard deviation of source isotopes (Stock et al., 2018). If the data is not normally distributed, it is challenging to characterize the source isotope features accurately using the MixSIAR model. In contrast, RFC models do not rely on the assumption of data normality.

The isotope fractionation during the processes of raw materials to emissions, as well as the post-emission processes, represents challenges in isotope tracing (Yin et al., 2014b). Current research on inorganic Hg (Hg(II) and Hg(0)) predominantly focuses on the oxidation-reduction, non-redox, and isotope exchange processes (Sun et al., 2016a; Zheng et al., 2019; Zheng and Hintelmann, 2009). These processes can induce significant MDF, indicating its susceptibility to physical and chemical reactions (Blum et al., 2014). For instance, the Hg(II) liquid-phase photo-reduction and dark reduction typically drive δ^{202}Hg of products in a negative shift (Rose et al., 2015). Isotope exchange processes may also yield notable MDF, but current studies are limited (Zheng et al., 2019). Previous studies reported that compared to feed coal, GEM and GOM in flue gas exhibited a significant enrichment of δ^{202}Hg (Tang et al., 2017), potential up to 0.3% enrichment (Sun et al., 2013a). Similarly, δ^{202}Hg was significantly enriched in the released PBM after biomass combustion, with δ^{202}Hg values ranging from −1.65‰ to −0.77‰ (Han et al., 2023). However, there is no unified pattern in δ^{202}Hg fractionation of Hg source materials before and after emissions, necessitating further study. Current research generally overlooks the impact of MDF on source attribution (Huang et al., 2016; Sun et al., 2021; Xu et al., 2017). Based on the current limited understanding, we choose not to incorporate δ^{202}Hg fractionation into the subsequent analysis of the source tracing model. Photochemical oxidation-reduction is the only known process that can result in significant odd-MIF, such as the liquid-phase photoreduction of Hg(II) (Blum et al., 2014). The photoreduction primarily contributes to atmospheric Hg transformation and typically causes a positive shift of Δ^{199}Hg influenced by atmospheric light intensity and residence time (Fu et al., 2019a). According to current understanding, it is generally believed that only intense photochemical redox in the troposphere can induce significant even-MIF, leading to the enrichment of Δ^{200}Hg in the products (Cai and Chen, 2016; Fu et al., 2021a). Therefore, Δ^{200}Hg can provide exclusive information about Hg sources due to being less affected by atmospheric processes. Raw materials and plants do not exhibit significant MIF during emitting Hg into the atmosphere through industrial or burning processes, displaying conservative MIF signals (Han et al., 2023; Huang et al., 2017; Yin et al., 2013c). Consequently, they can be characterized by MIF features of source materials (Sun et al., 2013a; Tang et al., 2017). In line with current knowledge, significant MIF in aerosols is typically triggered by intense atmospheric photochemical oxidation and reduction reactions during high-altitude transport. Hence, when tracing regional anthropogenic emissions, the impact of MIF can be disregarded. Alternatively, considering a reduction in the Δ^{199}Hg values of PBM is a viable option, but further investigation is imperative to determine the specific degree and range of MIF enrichment. Post-emission processes

are primarily influenced by homogenous atmospheric photochemical redox, causing isotope fractionation that mainly concentrates on atmospheric transport studies (Fu et al., 2019a; Yu et al., 2022). We undertook a detailed discussion of the isotopic fractionation of PBM in the subsequent section of atmospheric transport, excluding it from the analysis of contributions from anthropogenic sources.

3.2.3.2.2. Sources prediction. In this study, the RMC model based on machine learning was employed to quantify each emission source's contribution to PBM. Initially, we built the model using the δ^{202}Hg, Δ^{199}Hg, and Δ^{200}Hg values of potential emission sources, including lichen, moss, foliage/root, litter, coal rock, soil/dust, and Hg ore, mineral, and mineral waste, based on the bagging sampling method. The Hg isotope ratios and type of potential sources were set as the eigenvalues and target values of the RMC model, respectively. The RMC model was then taken to predict the probability of each source contributing to PBM based on the Hg isotopic composition of PBM. The employed RMC model on the training and out-of-bag datasets scored 0.64 and 0.60, respectively, indicating an accurate distinction of sources with a 60% probability based on δ^{202}Hg, Δ^{199}Hg, and Δ^{200}Hg values. The weights of eigenvalues δ^{202}Hg, Δ^{199}Hg, and Δ^{200}Hg to source classification were 51.16%, 38.23%, and 10.61%, respectively. As the sample size of various Hg sources is inconsistent, especially since some studies did not measure Δ^{200}Hg values, we also used the Synthetic Minority Oversampling Technique (SMOTE) method to balance the sample sizes before running the RMC model. The RMC model scored 0.85 and 0.74 on the training and out-of-bag datasets with sample size equalization using SMOTE, respectively. At this point, we can see that after equalizing the samples, the accuracy of MRC model predictions has increased by 14%. It is possible to infer that the RMC model can obtain higher fitting and prediction accuracy if the sample size is large enough. In other words, it can accurately identify the Hg source based on the Hg isotopes, demonstrating the reliability of using three-dimensional compositions of Hg isotopes to specify Hg sources.

We employed the RMC model with unprocessed datasets to predict PBM sources in China, as the RMC model exhibits a higher degree of overfitting to the training set after the data was processed using the SMOTE method. As Fig. 7 shows, coal is the most crucial contributor to atmospheric PBM in China, accounting for 38.42% of the total emissions, followed by Hg ore, mineral, and mineral waste (20.25%), soil/dust (17.14%), lichen (12.80%), litter (5.58%), rock (2.08%), moss (1.92%), and foliage/root (1.81%). Coal, Hg ore, mineral, and mineral waste, and soil/dust are the top three contributors to PBM, except for coastal areas. In coastal areas, vegetation such as lichen and litter is also a significant contributor to PBM, as a previous study reported that biomass burning was the primary contributor to PBM in the coastal area of Xiamen Bay, suggesting by the significantly negative Δ^{199}Hg values of PBM (Sun et al., 2021).

Industrial activities (coal and Hg ore, mineral, and mineral waste) are the primary contributors to PBM in China, accounting for 58.67%. Wu et al. (2016) also pointed out that the anthropogenic Hg emissions in China largely stem from coal combustion, metal smelting, and cement production. Biomass burning is another important source for PBM, contributing 22.11% of the total emissions to PBM. Combined with isotope ratios of PBM with elemental carbon and other aerosol compositions, Huang et al. (2016) found that coal combustion was the dominant factor influencing Beijing's PBM concentrations in winter, but biomass burning contributed the most in autumn. Moreover, a recent study conducted on the Tibetan Plateau showed that PBM accounted for 17.93% to 49.31% of Hg emitted from biomass combustion, which was considerably underestimated in previous studies (Han et al., 2023).

The contribution of soil/dust to PBM is underrated in previous studies. It reaches 17.14% of the total PBM emissions, ranging from 0.51% to 56.42%, as predicted by the RMC model in our study. The content of Hg in topsoil from Beijing can reach up to 7747 ng g^{-1}, proximate to the mass content of PBM (150–2200 ng g^{-1}) (Huang et al., 2016), suggesting that soil is probably one of the contributors to PBM (Qiu et al., 2021). Furthermore, Sun et al. (2020) found that the Hg contents of street dust in 60 cities in China ranged from 20 to 39,100 ng

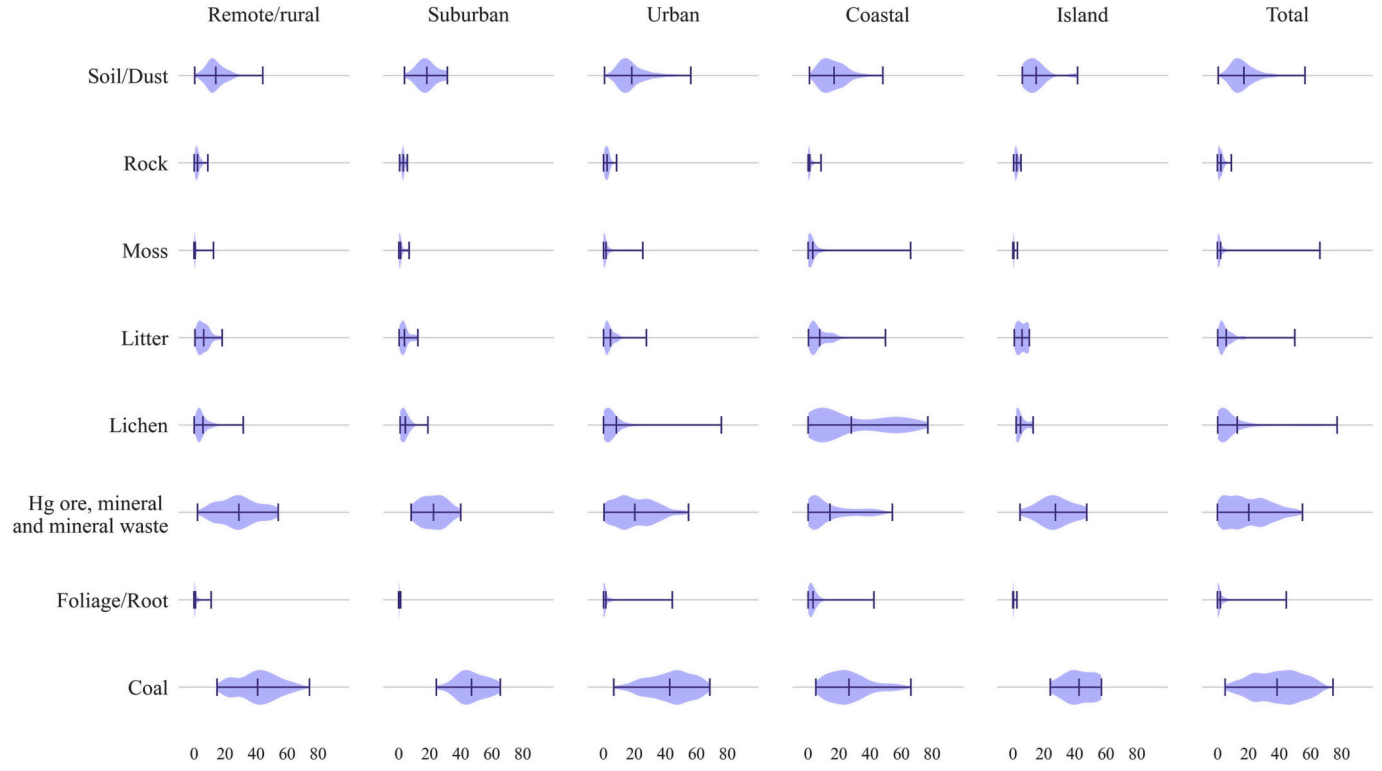

Fig. 7. Contributions (%) of various sources to PBM in China predicted by the random forest classifier model. Violin shapes represent data distributions, while the vertical line within each violine indicates the mean value. The upper and lower whiskers depict the maximum and minimum values. References for the dataset of Hg sources are provided in Fig. 4 and Fig. 6.

g^{-1}, and coal combustion and metal smelting were probably responsible for the high Hg concentration of dust in cities (Sun et al., 2020). Huang et al. (2020a) observed high PBM concentrations in the Taklimakan Desert, especially during dust storms, where the PBM content reached exceptionally high levels of hundreds or even thousands of nanograms per cubic meter. Additionally, dust adsorbing atmospheric Hg may cause significant increases in Hg concentrations in other regions of China through atmospheric transport (Huang et al., 2020a; Yu et al., 2019; Zhang et al., 2021a).

3.3. Atmospheric Hg transport

3.3.1. Atmospheric PBM transport in China

The East Asian monsoon (EAM), the Westerlies, and the Indian monsoon predominantly influence the air masses in China. The EAM, with the prevailing northwestern wind in winter and southeastern wind in summer, covers eastern China, including highly developed regions like the BTH region and Yangtze River Delta. The air masses in developing and sparsely populated western China are mainly impacted by the Westerlies and Indian monsoons, particularly in the Tibet Plateau region. The BTH region and its surrounding areas play a crucial role in investigating Chinese atmospheric Hg pollution. Because it is not only an important area of Hg emissions but also serves as a source of Hg that can be transported to other areas in eastern China, driven by the EAM (AMAP/UNEP, 2019; Qin et al., 2023; Wu et al., 2016). Regional emissions and atmospheric transport jointly influence the PBM concentration in the BTH region (Tang et al., 2019; Wang et al., 2021a). Beijing and its surrounding areas, such as Inner Mongolia, Hebei, Henan, and Shandong provinces, are the leading emitter of Hg in China (Wu et al., 2016), with coal combustion, biomass burning, non-ferrous metal smelting, and cement production being the primary sources (Huang et al., 2016; Qin et al., 2023). Under the influence of the EAM, air masses originating in Central Asia and Siberia would pass through Mongolia, Inner Mongolia, and other areas before arriving at the BTH region during spring, autumn, and winter. These air masses carry elevated PBM air masses through the surrounding cities and finally reach the BTH region during long-distance transport (Qin et al., 2023; Wang et al., 2021a). In addition, dust from deserts in the northwest can also act as a medium during PBM transport, further promoting the long-range transport of PBM from northwestern China to southeast China (Yu et al., 2019). However, during the East Asian summer monsoon, air masses originating from oceans carry relatively low levels of PBM and can scavenge PBM pollution in the BTH region (Qin et al., 2023).

Shanghai in the Yangtze River Delta is another frequently studied area for atmospheric PBM. The regional transport from Anhui, Jiangsu, Shandong, and Hebei, the primary Hg emitters located in the northwest of Shanghai, greatly impacts the PBM content in Shanghai during spring, autumn, and winter (Qin et al., 2019; Xiu et al., 2009). During the East Asian summer monsoon, the potential source areas of PBM in Shanghai are Zhejiang, Jiangxi, and Fujian (Qin et al., 2019; Xiu et al., 2009). Apart from regional transport, the long-range transport of air masses from the north driven by the winter monsoon also has a significant influence on PBM in Shanghai. These air masses carry elevated PBM content to Shanghai through Mongolia, Inner Mongolia, and the heavily polluted North China Plain, intensifying PBM pollution in the Yangtze River Delta (Hong et al., 2016b; Zhang et al., 2017). Alternatively, the ocean-cleaning air masses from the southeast are conducive to removing atmospheric particulate matter in this region (Cheng et al., 2017; Hong et al., 2016b). Research carried out at Huaniao Island, a remote site in the Yangtze River Delta, also shows that air masses from the north facilitated the increase of PBM concentrations in this area, especially when combined with desert dust during long-range transport (Duan et al., 2017a; Qin et al., 2016). Additionally, the airflow from the southeast ocean in summer may also increase PBM concentrations in Huaniao Island because of the oxidation of Hg^0 (Duan et al., 2017a).

The Hg circulation on the Tibet Plateau has attracted much attention due to its unique landforms. Unlike East China, which is affected by the EAM, the PBM transport over the Tibet Plateau is influenced by the Westerlies and the Indian monsoon. Due to the sparse population, atmospheric Hg concentrations on the Tibet Plateau are largely impacted by regional and long-range transport, such as domestic sources from Qinghai, Gansu, and Ningxia and transboundary sources from India, Nepal, Myanmar, and Bangladesh (Fu et al., 2012; Lin et al., 2019; Zhang et al., 2015; Zhang et al., 2021a). During transport, biomass burning, desert dust, and the photochemical transformation of Hg are the potential sources of PBM in the Tibet Plateau (Fu et al., 2019a; Zhang et al., 2015; Zhang et al., 2021a). For example, dust from the desert and Gobi areas contributes significantly to the PBM content at the WLG station under the westerlies-driven long-range transport (Zhang et al., 2021a). Moreover, the glacial winds shaped by glaciers on the Tibet plateau pump air masses from the upper atmosphere to the surface, likely intensifying air mass transport and causing PBM pollution (Lin et al., 2019).

Some studies also have studied the atmospheric PBM transport in other regions of China, most of which were conducted in eastern China. Wang et al. (2020) showed that the atmospheric PBM in Changdao island of Shandong Province was affected by the long-range transport from North China, and atmospheric fine particles were easier to absorb atmospheric Hg and be transported over long distances. Similarly, research in Xiamen shows that its potential source areas were mainly located in the coastal and inland cities of eastern China affected by the EAM, while air masses from the South China Sea and the western Pacific in summer brought clean air mass (Xu et al., 2015). Liu et al. (2019a) demonstrated that the MCB station located in the remote Changbai Mountains was more likely to be impacted by the long-range transport of PBM emitted by humans in northeast and east China and the large-scale biomass burning in northeast Asia. In general, due to the impact of the EAM, the North China Plain is the crucial region for Hg pollution and transport to other regions in China.

3.3.2. Hg isotopes tracing PBM transport

Previous studies generally demonstrated the potential sources of PBM by combining Hg content and meteorological data with the Potential Source Contribution Function (PSCF) model (Cheng et al., 2015; Dieguez et al., 2019; Zhang et al., 2021b). However, the contributions of regional emissions and long-distance transport have not been clearly differentiated. Thanks to advancements in high-precision measurements, Hg isotopes, characterized by unique three-dimensional fractionation, offer new insights into revealing Hg emissions and tracing Hg transport (Ariya et al., 2015; Blum and Bergquist, 2007; Blum et al., 2014). The PBM in China presents a broad range of isotopic compositions, with δ^{202}Hg ranging from $> -3.7‰$ to $<1.2‰$ and Δ^{199}Hg ranging from > -1.4 to <1.5 (Fig. 6). Previous studies have reported that isotopic signatures of anthropogenic sources generally showed negative values for δ^{202}Hg and near-zero or negative values for Δ^{199}Hg (Huang et al., 2016; Qin et al., 2023; Sun et al., 2016b; Yin et al., 2014a). The majority of δ^{202}Hg values of PBM in remote/rural, suburban, and urban areas are negative. However, some Δ^{199}Hg values of PBM in those areas are significantly positive instead of near-zero or negative values, suggesting that others, such as atmospheric transport, have a greater influence on PBM than regional anthropogenic sources. During atmospheric transport, Hg shows elevated Δ^{199}Hg values under photochemical redox processes (Chen et al., 2012; Fu et al., 2019a; Qiu et al., 2021). Therefore, PBM would present higher Δ^{199}Hg values when long-range transport of atmospheric Hg contributed significantly. For instance, many Δ^{199}Hg values of PBM in remote/rural areas and islands are positive (Fig. 6), suggesting the combined influences of regional anthropogenic emissions and long-range transports. However, regional anthropogenic emission is more critical in PBM levels than long-range transport in other areas, such as suburban, urban, and coastal areas, as they exhibit lower Δ^{199}Hg values, close to the isotope ratios of emission sources (Fig. 6). For instance, Sun et al. (2021) identified biomass

burning as the primary contributor to PBM in the coastal area of Xiamen based on noticeably negative Δ^{199}Hg, and in autumn, near zero Δ^{199}Hg values and elevated Hg concentrations indicated a significant contribution from regional anthropogenic emissions. Additionally, due to intensively anthropogenic activities, industrial emissions tend to be the predominant factors affecting PBM content in urban Beijing areas (Huang et al., 2016).

Research conducted in Kolkata, India, reported that the Δ^{199}Hg values of PBM varied from −0.31 ‰ to +0.33 ‰ (Das et al., 2016). Summer air masses originating from the Bay of Bengal greatly contributed to forming PBM, promoting the enrichment of Δ^{199}Hg; in contrast, during winter, northern dust predominantly influenced PBM (Das et al., 2016). MIF was mostly negative in another area with severe PBM pollution in the Indo-Gangetic Plain, with local emissions dominating PBM formation (Guo et al., 2021). However, in the Arctic region, Hg content was markedly affected by Hg emissions from the Northern Hemisphere, atmospheric Hg dissipation events, and re-emissions (Angot et al., 2016). Zheng et al. (2021) pointed out that PBM in the Arctic region exhibited negative $\triangle^{199}$Hg values, different from the positive $\triangle^{199}$Hg values commonly found in oxidized-Hg forms elsewhere. They believe that PBM was mainly derived from the in-situ oxidation of GEM and subsequent particle scavenging, thus inheriting the isotopic ratios of GEM rather than directly from the long-distance transport of PBM from anthropogenic emissions (Zheng et al., 2021).

Combining Hg isotopic compositions and PSCF has also been employed to invert atmospheric Hg transport processes in studies (Qin et al., 2023; Yu et al., 2022). Due to the stability of Δ^{199}Hg, generally triggered by photochemical reactions, Yu et al. (2022) combined high and low Δ^{199}Hg values with the PSCF model to identify anthropogenic emission areas and background transport areas of TGM in the Tibet Plateau, respectively. When using high Δ^{199}Hg values to trace PBM transport, it should be noted that water-soluble organic carbon may significantly elevate Δ^{199}Hg values by photoreduction during severely polluted and high relative humidity weather (Zhang et al., 2022). More studies on the laws and mechanisms of Hg isotope fractionations are needed to disclose the geochemical process of atmospheric Hg.

3.4. Conclusions, implications, and future research direction

This review summarized the PBM spatial and temporal variations across China, revealed Hg circulation by combining the Hg isotope dataset and SEM, and identified the contributions of anthropogenic sources to PBM using Hg isotopes and machine learning. The findings offer valuable insights into the sources, transformation, and circulation of atmospheric Hg:

(1) The median concentrations of PBM_{TSP} and $PBM_{2.5}$ in China are 74.5 and 273.6 pg m^{-3}, respectively, and the $PBM_{2.5}/PBM_{TSP}$ ratio ranges from 35.7% to 72.5%. Urban areas have the highest mean PBM concentration, followed by suburban, coastal, remote/rural, and island areas. Moreover, the developed cities in eastern China present higher PBM concentrations than in western China, indicating significant contributions of anthropogenic emissions to PBM. PBM concentrations are higher in northern China than in southern China for both monthly and seasonal variations, indicating that, besides heating, other factors like temperature, humidity, planetary boundary layer, and atmospheric transmission significantly contribute to atmospheric PBM. The long-term annual variation of PBM concentrations in China shows an initial increase followed by a decrease, with a significant decline observed since 2015. Based on PCA-MLR results, anthropogenic sources, atmospheric transport, and atmospheric process contribute 56.2%, 14.9%, and 29.0%, respectively, to the PBM content in China.

(2) The range of Hg isotope fractionation of natural materials in the environment is broad: δ^{202}Hg > 8.44‰, Δ^{199}Hg > 12.67‰, Δ^{200}Hg > 1.45‰. The δ^{202}Hg and Δ^{199}Hg isotope ratios of atmospheric Hg samples primarily coincide with those of solid natural materials and vegetation. The results of the SEM exhibit significant relationships ($P < 0.01$) between atmospheric Hg and Hg raw materials (0.91) and vegetation (1.78), suggesting that they contribute significantly to atmospheric Hg. Hg in the atmosphere and in water and fish have significant ($P < 0.01$) effects on humans, and the regression coefficient between atmospheric Hg and humans is higher, indicating that direct inhalation of Hg from the atmosphere should be a concern. In addition, atmospheric Hg deposition significantly impacts ($P < 0.01$) the Hg isotope compositions of water and fish, and the deposited Hg subsequently accumulates in sediments.

(3) PBM in China mostly has negative δ^{202}Hg and near-zero Δ^{199}Hg values, overlapping with most Hg emission sources. The highest Δ^{199}Hg value of PBM is observed in remote/rural areas, followed by islands, suburban, urban, and coastal areas. The Δ^{199}Hg $/\Delta^{201}$Hg ratio of PBM in China is 1.11 ± 0.02, indicating that atmospheric Hg primarily undergoes photoreduction reactions. According to the linearized binary isotope mixing equation, the estimated δ^{202}Hg and Δ^{199}Hg values of anthropogenic sources affecting PBM are −0.79‰ and 0.02%, respectively. We employed the RMC model to predict the contribution of each emission source to PBM. Coal is the most important contributor to China's atmospheric PBM, accounting for 38.42% of total emissions, followed by Hg ore, mineral, and mineral waste (20.25%), soil/dust (17.14%), lichen (12.80%), litter (5.58%), rock (2.08%), moss (1.92%), and foliage/root (1.81%). It should be noted that the contribution of soil/dust to PBM is underestimated in previous studies as it ranges from 0.51% to 56.42%.

(4) The EAM primarily influences PBM transport in eastern China. The BTH region and its surrounding areas are crucial in studying atmospheric Hg pollution, as it is not only a heavy Hg emission area but also affects other areas by the EAM. Western China is mainly affected by the Westerlies and the Indian monsoon. During atmospheric transport, PBM exhibits elevated Δ^{199}Hg and Δ^{200}Hg values, generally triggered by photochemical redox processes (Chen et al., 2012; Fu et al., 2019a; Qiu et al., 2021). Combining Hg isotopes and PSCF has been used to invert atmospheric Hg transport processes (Qin et al., 2023; Yu et al., 2022). The Δ^{199}Hg values for remote/rural and island PBM are mostly positive, indicating the combined effects of regional anthropogenic emissions and long-range transport. However, regional anthropogenic emissions have a greater influence on PBM in other areas.

Overall, atmospheric PBM in China has significantly decreased after 2015 compared to the previous increasing trend, indicating the effective implementation of the Minamata Convention on Mercury. However, China's PBM concentration remains higher than developed countries, suggesting further space for reduction. Additionally, PBM can be transported from key emission regions like the North China Plain to other areas within China and even globally under the influence of monsoons.

In the present study, China's PBM observation sites are insufficient, with most located in developed cities. Furthermore, there need to be adequate long-term atmospheric Hg observation sites, which hinders the accurate assessment of PBM concentration trends in China. Our research reveals that with sufficient Hg isotopic data, the RMC model's classification ability for Hg sources will greatly improve, demonstrating the feasibility of machine learning combined with Hg isotopic tracing and highlighting the importance of further studying Hg isotopic compositions of natural materials. Further research on the mechanisms behind Hg isotope fractionation can offer valuable insights into determining the geochemical cycle of Hg. For instance, Hg isotopes (Δ^{199}Hg, Δ^{200}Hg) can indicate atmospheric PBM transport, but quantifying regional Hg

transport using Hg isotopes remains challenging. It is advisable that future research concentrates on both monitoring and modeling atmospheric Hg patterns and fractionation to understand better Hg geochemical circulation impacts on human health and the environment.

Declaration of competing interest

The authors declare that they have no known competing financial interests or personal relationships that could have appeared to influence the work reported in this paper.

Data availability

Data will be made available on request.

Acknowledgments

This study was funded by the National Key Research and Development Program of China (No. 2017YFC0212703), the National Natural Science Foundation of China (Grant Nos. 41625006, 41761144066, 41561144005, 41890824, 41890822), and the Cross-Team and Key Laboratory Cooperative Research Special Project of Chinese Academy of Sciences (CAS "Light of West China" Program). Xuechao Qin is personally funded by the China Scholarship Council (No. 202104910111).

Appendix A. Supplementary data

Supplementary data to this article can be found online at https://doi.org/10.1016/j.earscirev.2024.104681.

References

AMAP/UNEP, 2013. Technical Background Report for the Global Mercury Assessment 2013. Arctic Monitoring and Assessment Programme, Oslo, Norway/UNEP Chemicals Branch, Geneva, Switzerland.
AMAP/UNEP, 2019. Technical Background Report for the Global Mercury Assessment 2018. Arctic Monitoring and Assessment Programme, Oslo,. Norway/UNEP, Chemicals and Health Branch, Geneva, Switzerland.
Angot, H., Dastoor, A., De Simone, F., Gardfeldt, K., Gencarelli, C.N., Hedgecock, I.M., Langer, S., Magand, O., Mastromonaco, M.N., Nordstrom, C., Pfaffhuber, K.A., Pirrone, N., Ryjkov, A., Selin, N.E., Skov, H., Song, S.J., Sprovieri, F., Steffen, A., Toyota, K., Travnikov, O., Yang, X., Dommergue, A., 2016. Chemical cycling and deposition of atmospheric mercury in polar regions: review of recent measurements and comparison with models. Atmos. Chem. Phys. 16 (16), 10735–10763.
Araujo, B.F., Osterwalder, S., Szponar, N., Lee, D., Petrova, M.V., Pernov, J.B., Ahmed, S., Heimbürger-Boavida, L.-E., Laffont, L., Teisserenc, R., 2022. Mercury isotope evidence for Arctic summertime re-emission of mercury from the cryosphere. Nat. Commun. 13 (1), 4956.
Ariya, P.A., Amyot, M., Dastoor, A., Deeds, D., Feinberg, A., Kos, G., Poulain, A., Ryjkov, A., Semeniuk, K., Subir, M., Toyota, K., 2015. Mercury physicochemical and biogeochemical transformation in the atmosphere and at atmospheric interfaces: a review and future directions. Chem. Rev. 115 (10), 3760–3802.
Bergquist, B.A., Blum, J.D., 2007. Mass-dependent and -independent fractionation of hg isotopes by photoreduction in aquatic systems. Science 318 (5849), 417–420.
Biswas, A., Blum, J.D., Bergquist, B.A., Keeler, G.J., Xie, Z., 2008. Natural mercury isotope variation in coal deposits and organic soils. Environ. Sci. Technol. 42 (22), 8303–8309.
Blanchard, P., Froude, F.A., Martin, J.B., Dryfhout-Clark, H., Woods, J.T., 2002. Four years of continuous total gaseous mercury (TGM) measurements at sites in Ontario, Canada. Atmos. Environ. 36 (23), 3735–3743.
Blanchfield, P.J., Rudd, J.W., Hrenchuk, L.E., Amyot, M., Babiarz, C.L., Beaty, K.G., Bodaly, R.D., Branfireun, B.A., Gilmour, C.C., Graydon, J.A., 2022. Experimental evidence for recovery of mercury-contaminated fish populations. Nature 601 (7891), 74–78.
Blum, J.D., Bergquist, B.A., 2007. Reporting of variations in the natural isotopic composition of mercury. Anal. Bioanal. Chem. 388 (2), 353–359.
Blum, J.D., Johnson, M.W., 2017. Recent Developments in Mercury Stable Isotope Analysis. Rev. Mineral. Geochem. 82 (1), 733–757.
Blum, J.D., Sherman, L.S., Johnson, M.W., 2014. Mercury Isotopes in Earth and Environmental Sciences. Annu. Rev. Earth Planet. Sci. 42 (1), 249–269.
Božič, D., Živković, I., Hudobivnik, M.J., Kotnik, J., Amouroux, D., Štrok, M., Horvat, M., 2022. Fractionation of mercury stable isotopes in lichens. Chemosphere 309, 136592.
Cai, H., Chen, J., 2016. Mass-independent fractionation of even mercury isotopes. Sci. Bull. 61 (2), 116–124.
Carignan, J., Estrade, N., Sonke, J.E., Donard, O.F.X., 2009. Odd Isotope Deficits in Atmospheric Hg measured in Lichens. Environ. Sci. Technol. 43 (15), 5660–5664.
Chen, J.B., Hintelmann, H., Feng, X.B., Dimock, B., 2012. Unusual fractionation of both odd and even mercury isotopes in precipitation from Peterborough, ON, Canada. Geochim. Cosmochim. Acta 90, 33–46.
Chen, L., Liu, M., Xu, Z., Fan, R., Tao, J., Chen, D., Zhang, D., Xie, D., Sun, J., 2013. Variation trends and influencing factors of total gaseous mercury in the Pearl River Delta—A highly industrialised region in South China influenced by seasonal monsoons. Atmos. Environ. 77, 757–766.
Chen, X.J., Balasubramanian, R., Zhu, Q.Y., Behera, S.N., Bo, D.D., Huang, X., Xie, H.Y., Cheng, J.P., 2016. Characteristics of atmospheric particulate mercury in size-fractionated particles during haze days in Shanghai. Atmos. Environ. 131, 400–408.
Cheng, I., Xu, X., Zhang, L., 2015. Overview of receptor-based source apportionment studies for speciated atmospheric mercury. Atmos. Chem. Phys. 15 (14), 7877–7895.
Cheng, N., Duan, L., Xiu, G.L., Zhao, M.F., Qian, G.L., 2017. Comparison of atmospheric PM2.5-bounded mercury species and their correlation with bromine and iodine at coastal urban and island sites in the eastern China. Atmos. Res. 183, 17–25.
Cole, A.S., Steffen, A., Pfaffhuber, K.A., Berg, T., Pilote, M., Poissant, L., Tordon, R., Hung, H., 2013. Ten-year trends of atmospheric mercury in the high Arctic compared to Canadian sub-Arctic and mid-latitude sites. Atmos. Chem. Phys. 13 (3), 1535–1545.
Cole, A.S., Steffen, A., Eckley, C.S., Narayan, J., Pilote, M., Tordon, R., Graydon, J.A., Louis, V.L., Xu, X., Branfireun, B.A., 2014. A survey of mercury in air and precipitation across Canada: patterns and trends. Atmosphere 5 (3), 635–668.
Cooke, C.A., Hintelmann, H., Ague, J.J., Burger, R., Biester, H., Sachs, J.P., Engstrom, D. R., 2013. Use and legacy of mercury in the Andes. Environ. Sci. Technol. 47 (9), 4181–4188.
Das, R., Wang, X., Khezri, B., Webster, R.D., Sikdar, P.K., Datta, S., Blum, J.D., Hintelmann, H., 2016. Mercury isotopes of atmospheric particle bound mercury for source apportionment study in urban Kolkata, India. In: Elementa: Science of the Anthropocene, p. 4.
Demers, J.D., Blum, J.D., Zak, D.R., 2013. Mercury isotopes in a forested ecosystem: Implications for air-surface exchange dynamics and the global mercury cycle. Glob. Biogeochem. Cycles 27 (1), 222–238.
Dieguez, M.C., Bencardino, M., Garcia, P.E., D'Amore, F., Castagna, J., De'Simone, F., Cardenas, C.S., Guevara, S.R., Pirrone, N., Sprovieri, F., 2019. A multi-year record of atmospheric mercury species at a background mountain station in Andean Patagoliia (Argentina): Temporal trends and meteorological influence. Atmos. Environ. 214.
Donovan, P.M., Blum, J.D., Yee, D., Gehrke, G.E., Singer, M.B., 2013. An isotopic record of mercury in San Francisco Bay sediment. Chem. Geol. 349, 87–98.
Driscoll, C.T., Mason, R.P., Chan, H.M., Jacob, D.J., Pirrone, N., 2013. Mercury as a global pollutant: sources, pathways, and effects. Environ. Sci. Technol. 47 (10), 4967–4983.
Du, B., Feng, X., Li, P., Yin, R., Yu, B., Sonke, J.E., Guinot, B., Anderson, C.W.N., Maurice, L., 2018. Use of mercury isotopes to quantify mercury exposure sources in Inland Populations, China. Environ. Sci. Technol. 52 (9), 5407–5416.
Du, H., Wang, X., Yuan, W., Wu, F., Jia, L., Liu, N., Lin, C.J., Gan, J., Zeng, F., Wang, K., Feng, X., 2023. Elevated Mercury Deposition, Accumulation, and Migration in a Karst Forest. Environ Sci Technol 57 (45), 17490–17500.
Du, B., Yin, R., Fu, X., Li, P., Feng, X., Maurice, L., 2021. Use of mercury isotopes to quantify sources of human inorganic mercury exposure and metabolic processes in the human body. Environ. Int. 147, 106336.
Duan, L., Xiu, G.L., Feng, L., Cheng, N., Wang, C.G., 2016. The mercury species and their association with carbonaceous compositions, bromine and iodine in PM2.5 in Shanghai. Chemosphere 146, 263–271.
Duan, L., Cheng, N., Xiu, G.L., Wang, F.J., Chen, Y., 2017a. Characteristics and source appointment of atmospheric particulate mercury over East China Sea: Implication on the deposition of atmospheric particulate mercury in marine environment. Environ. Pollut. 224, 26–34.
Duan, L., Wang, X.H., Wang, D.F., Duan, Y.S., Cheng, N., Xiu, G.L., 2017b. Atmospheric mercury speciation in Shanghai, China. Sci. Total Environ. 578, 460–468.
Estrade, N., Carignan, J., Sonke, J.E., Donard, O.F.X., 2009. Mercury isotope fractionation during liquid–vapor evaporation experiments. Geochim. Cosmochim. Acta 73 (10), 2693–2711.
Estrade, N., Carignan, J., Donard, O.F.X., 2010. Isotope tracing of atmospheric mercury sources in an urban area of Northeastern France. Environ. Sci. Technol. 44 (16), 6062–6067.
Estrade, N., Carignan, J., Donard, O.F., 2011. Tracing and quantifying anthropogenic mercury sources in soils of northern France using isotopic signatures. Environ. Sci. Technol. 45 (4), 1235–1242.
Fain, X., Obrist, D., Hallar, A.G., McCubbin, I., Rahn, T., 2009. High levels of reactive gaseous mercury observed at a high elevation research laboratory in the Rocky Mountains. Atmos. Chem. Phys. 9 (20), 8049–8060.
Feng, X.B., Shang, L.H., Wang, S.F., Tang, S.L., Zheng, W., 2004. Temporal variation of total gaseous mercury in the air of Guiyang, China. J. Geophys. Res.-Atmos. 109 (D3).
Feng, X., Chen, Y., Du, H., Feng, Y., Mu, Y., Chen, J., 2023. Biomass burning is a non-negligible source for ammonium during winter haze episodes in rural North China: evidence from high time resolution 15N-stable isotope. J. Geophys. Res. Atmos. 128 (3).
Foucher, D., Hintelmann, H., 2009. Tracing mercury contamination from the Idrija mining region (Slovenia) to the Gulf of Trieste using Hg isotope ratio measurements. Environ. Sci. Technol. 43 (1), 33–39.
Fu, X.W., Feng, X., Liang, P., Deliger, Zhang, H., Ji, J. and Liu, P., 2012. Temporal trend and sources of speciated atmospheric mercury at Waliguan GAW station, Northwestern China. Atmos. Chem. Phys. 12 (4), 1951–1964.

Fu, X.W., Zhang, H., Lin, C.J., Feng, X.B., Zhou, L.X., Fang, S.X., 2015. Correlation slopes of GEM/CO, GEM/CO2, and GEM/CH4 and estimated mercury emissions in China, South Asia, the Indochinese Peninsula, and Central Asia derived from observations in northwestern and southwestern China. Atmos. Chem. Phys. 15 (2), 1013–1028.
Fu, X., Marusczak, N., Wang, X., Gheusi, F., Sonke, J.E., 2016a. Isotopic composition of gaseous elemental mercury in the free troposphere of the Pic du Midi Observatory, France. Environ. Sci. Technol. 50 (11), 5641–5650.
Fu, X., Zhu, W., Zhang, H., Sommar, J., Yu, B., Yang, X., Wang, X., Lin, C.-J., Feng, X., 2016b. Depletion of atmospheric gaseous elemental mercury by plant uptake at Mt. Changbai, Northeast China. Atmos. Chem. Phys. 16 (20), 12861–12873.
Fu, X.W., Yang, X., Tan, Q.Y., Ming, L.L., Lin, T., Lin, C.J., Li, X.D., Feng, X.B., 2018. Isotopic composition of gaseous elemental mercury in the boundary layer of East China Sea. J. Geophys. Res.-Atmos. 123 (14), 7656–7669.
Fu, X.W., Zhang, H., Feng, X.B., Tan, Q.Y., Ming, L.L., Liu, C., Zhang, L.M., 2019a. Domestic and transboundary sources of atmospheric particulate bound mercury in remote areas of China: evidence from mercury isotopes. Environ. Sci. Technol. 53 (4), 1947–1957.
Fu, X.W., Zhang, H., Liu, C., Zhang, H., Lin, C.J., Feng, X.B., 2019b. Significant seasonal variations in isotopic composition of atmospheric total gaseous mercury at forest sites in China caused by vegetation and mercury sources. Environ. Sci. Technol. 53 (23), 13748–13756.
Fu, X.W., Jiskra, M., Yang, X., Marusczak, N., Enrico, M., Chmeleff, J., Heimburger-Boavida, L.E., Gheusi, F., Sonke, J.E., 2021a. Mass-independent fractionation of even and odd mercury isotopes during atmospheric mercury redox reactions. Environ. Sci. Technol. 55 (14), 10164–10174.
Fu, X.W., Liu, C., Zhang, H., Xu, Y., Li, J., Lyu, X.P., Zhang, G., Guo, H., Wang, X., Zhang, L.M., Feng, X.B., 2021b. Isotopic compositions of atmospheric total gaseous mercury in 10 Chinese cities and implications for land surface emissions. Atmos. Chem. Phys. 21 (9), 6721–6734.
Gantner, N., Hintelmann, H., Zheng, W., Muir, D.C., 2009. Variations in stable isotope fractionation of Hg in food webs of Arctic lakes. Environ. Sci. Technol. 43 (24), 9148–9154.
Gehrke, G.E., Blum, J.D., Marvin-DiPasquale, M., 2011a. Sources of mercury to San Francisco Bay surface sediment as revealed by mercury stable isotopes. Geochim. Cosmochim. Acta 75 (3), 691–705.
Gehrke, G.E., Blum, J.D., Slotton, D.G., Greenfield, B.K., 2011b. Mercury isotopes link mercury in San Francisco Bay forage fish to surface sediments. Environ. Sci. Technol. 45 (4), 1264–1270.
Gratz, L.E., Keeler, G.J., Blum, J.D., Sherman, L.S., 2010. Isotopic composition and fractionation of mercury in Great Lakes precipitation and ambient air. Environ. Sci. Technol. 44 (20), 7764–7770.
Guo, J.M., Sharma, C.M., Tripathee, L., Kang, S.C., Fu, X.W., Huang, J., Shrestha, K.L., Chen, P.F., 2021. Source identification of atmospheric particle-bound mercury in the Himalayan foothills through non-isotopic and isotope analyses*. Environ. Pollut. 286, 117317.
Han, D., Wu, Q., Wen, M., Tang, Y., Li, G., Ren, Y., Cui, Y., Li, Z., Shi, J., Zhang, Q., Yin, X., Wang, S., 2023. Isotopic fractionation characteristics of speciated mercury from local biomass combustion in the Tibetan Plateau. Environ. Sci. Technol. 57 (12), 4775–4783.
Hatcher, P.G., Clifford, D.J., 1997. The organic geochemistry of coal: from plant materials to coal. Org. Geochem. 27 (5), 251–274.
He, K., Yang, F., Ma, Y., Zhang, Q., Yao, X., Chan, C.K., Cadle, S., Chan, T., Mulawa, P., 2001. The characteristics of PM2. 5 in Beijing, China. Atmos. Environ. 35 (29), 4959–4970.
Holmes, C.D., Jacob, D.J., Mason, R.P., Jaffe, D.A., 2009. Sources and deposition of reactive gaseous mercury in the marine atmosphere. Atmos. Environ. 43 (14), 2278–2285.
Hong, Q.Q., Xie, Z.Q., Liu, C., Wang, F.Y., Xie, P.H., Kang, H., Xu, J., Wang, J.C., Wu, F. C., He, P.Z., Mou, F.S., Fan, S.D., Dong, Y.S., Zhan, H.C., Yu, X.W., Chi, X.Y., Liu, J. G., 2016a. Speciated atmospheric mercury on haze and non-haze days in an inland city in China. Atmos. Chem. Phys. 16 (21), 13807–13821.
Hong, Y.W., Chen, J.S., Deng, J.J., Tong, L., Xu, L.L., Niu, Z.C., Yin, L.Q., Chen, Y.T., Hong, Z.Y., 2016b. Pattern of atmospheric mercury speciation during episodes of elevated PM2.5 levels in a coastal city in the Yangtze River Delta, China. Environ. Pollut. 218, 259–268.
Horowitz, H.M., Jacob, D.J., Zhang, Y.X., Dibble, T.S., Slemr, F., Amos, H.M., Schmidt, J. A., Corbitt, E.S., Marais, E.A., Sunderland, E.M., 2017. A new mechanism for atmospheric mercury redox chemistry: implications for the global mercury budget. Atmos. Chem. Phys. 17 (10), 6353–6371.
Howard, D., Edwards, G.C., 2018. Mercury fluxes over an Australian alpine grassland and observation of nocturnal atmospheric mercury depletion events. Atmos. Chem. Phys. 18 (1), 129–142.
Huang, S., Yuan, D., Lin, H., Sun, L., Lin, S., 2017. Fractionation of mercury stable isotopes during coal combustion and seawater flue gas desulfurization. Appl. Geochem. 76, 159–167.
Huang, R.J., Zhang, Y.L., Bozzetti, C., Ho, K.F., Cao, J.J., Han, Y.M., Daellenbach, K.R., Slowik, J.G., Platt, S.M., Canonaco, F., Zotter, P., Wolf, R., Pieber, S.M., Bruns, E.A., Crippa, M., Ciarelli, G., Piazzalunga, A., Schwikowski, M., Abbaszade, G., Schnelle-Kreis, J., Zimmermann, R., An, Z.S., Szidat, S., Baltensperger, U., El Haddad, I., Prevot, A.S.H., 2014. High secondary aerosol contribution to particulate pollution during haze events in China. Nature 514 (7521), 218–222.
Huang, Q., Chen, J.B., Huang, W.L., Fu, P.Q., Guinot, B., Feng, X.B., Shang, L.H., Wang, Z.H., Wang, Z.W., Yuan, S.L., Cai, H.M., Wei, L.F., Yu, B., 2016. Isotopic composition for source identification of mercury in atmospheric fine particles. Atmos. Chem. Phys. 16 (18), 11773–11786.
Huang, S., Yuan, D., Lin, H., Sun, L., Lin, S., 2017. Fractionation of mercury stable isotopes during coal combustion and seawater flue gas desulfurization. Appl. Geochem. 76, 159–167.
Huang, Q., Chen, J.B., Huang, W.L., Reinfelder, J.R., Fu, P.Q., Yuan, S.L., Wang, Z.W., Yuan, W., Cai, H.M., Ren, H., Sun, Y.L., He, L., 2019. Diel variation in mercury stable isotope ratios records photoreduction of PM2.5-bound mercury. Atmos. Chem. Phys. 19 (1), 315–325.
Huang, J., Kang, S.C., Yin, R.S., Ram, K., Liu, X.C., Lu, H., Guo, J.M., Chen, S.Y., Tripathee, L., 2020a. Desert dust as a significant carrier of atmospheric mercury. Environ. Pollut. 267.
Huang, Q., Reinfelder, J.R., Fu, P.Q., Huang, W.L., 2020b. Variation in the mercury concentration and stable isotope composition of atmospheric total suspended particles in Beijing, China. J. Hazard. Mater. 383.
Jiskra, M., Wiederhold, J.G., Skyllberg, U., Kronberg, R.-M., Hajdas, I., Kretzschmar, R., 2015. Mercury deposition and re-emission pathways in boreal forest soils investigated with Hg isotope signatures. Environ. Sci. Technol. 49 (12), 7188–7196.
Jiskra, M., Wiederhold, J.G., Skyllberg, U., Kronberg, R.M., Kretzschmar, R., 2017. Source tracing of natural organic matter bound mercury in boreal forest runoff with mercury stable isotopes. Environ. Sci. Process. Impacts 19 (10), 1235–1248.
Jiskra, M., Sonke, J.E., Agnan, Y., Helmig, D., Obrist, D., 2019. Insights from mercury stable isotopes on terrestrial–atmosphere exchange of Hg (0) in the Arctic tundra. Biogeosciences 16 (20), 4051–4064.
Jiskra, M., Wiederhold, J.G., Skyllberg, U., Kronberg, R.M., Kretzschmar, R., 2017. Source tracing of natural organic matter bound mercury in boreal forest runoff with mercury stable isotopes. Environ. Sci.: Processes Impacts 19 (10), 1235–1248.
Kritee, K., Motta, L.C., Blum, J.D., Tsui, M.T.-K., Reinfelder, J.R., 2018. Photomicrobial visible light-induced magnetic mass independent fractionation of mercury in a marine microalga. ACS Earth Space Chem. 2 (5), 432–440.
Laffont, L., Sonke, J.E., Maurice, L., Hintelmann, H., Pouilly, M., Sánchez Bacarreza, Y., Perez, T., Behra, P., 2009. Anomalous mercury isotopic compositions of fish and human hair in the Bolivian Amazon. Environ. Sci. Technol. 43 (23), 8985–8990.
Landis, M.S., Lewis, C.W., Stevens, R.K., Keeler, G.J., Dvonch, J.T., Tremblay, R.T., 2007. Ft. McHenry tunnel study: source profiles and mercury emissions from diesel and gasoline powered vehicles. Atmos. Environ. 41 (38), 8711–8724.
Lee, D.S., Dollard, G.J., Pepler, S., 1998. Gas-phase mercury in the atmosphere of the United Kingdom. Atmos. Environ. 32 (5), 855–864.
Lefticariu, L., Blum, J.D., Gleason, J.D., 2011. Mercury isotopic evidence for multiple mercury sources in coal from the Illinois basin. Environ. Sci. Technol. 45 (4), 1724–1729.
Lepak, R.F., Yin, R., Krabbenhoft, D.P., Ogorek, J.M., DeWild, J.F., Holsen, T.M., Hurley, J.P., 2015. Use of stable isotope signatures to determine mercury sources in the Great Lakes. Environ. Sci. Technol. Lett. 2 (12), 335–341.
Lepak, R.F., Ogorek, J.M., Bartz, K.K., Janssen, S.E., Tate, M.T., Runsheng, Y., Hurley, J. P., Young, D.B., Eagles-Smith, C.A., Krabbenhoft, D.P., 2022. Using carbon, nitrogen, and mercury isotope values to distinguish mercury sources to Alaskan lake trout. Environ. Sci. Technol. Lett. 9 (4), 312–319.
Li, M., Sherman, L.S., Blum, J.D., Grandjean, P., Mikkelsen, B., Weihe, P.L., Sunderland, E.M., Shine, J.P., 2014. Assessing sources of human methylmercury exposure using stable mercury isotopes. Environ. Sci. Technol. 48 (15), 8800–8806.
Li, M., von Stackelberg, K., Rheinberger, C.M., Hammitt, J.K., Krabbenhoft, D.P., Yin, R., Sunderland, E.M., 2016. Insights from mercury stable isotopes into factors affecting the internal body burden of methylmercury in frequent fish consumersMercury stable isotopes in frequent fish consumers. In: Elementa: Science of the Anthropocene, p. 4.
Li, P., Du, B., Maurice, L., Laffont, L., Lagane, C., Point, D., Sonke, J.E., Yin, R., Lin, C.-J., Feng, X., 2017. Mercury isotope signatures of methylmercury in rice samples from the Wanshan mercury mining area, China: environmental implications. Environ. Sci. Technol. 51 (21), 12321–12328.
Li, C.J., Chen, J.B., Angot, H., Zheng, W., Shi, G.T., Ding, M.H., Du, Z.H., Zhang, Q.G., Ma, X.Y., Kang, S.C., Xiao, C.D., Ren, J.W., Qin, D.H., 2020. Seasonal variation of mercury and its isotopes in atmospheric particles at the Coastal Zhongshan Station, Eastern Antarctica. Environ. Sci. Technol. 54 (18), 11344–11355.
Li, M.L., Kwon, S.Y., Poulin, B.A., Tsui, M.T., Motta, L.C., Cho, M., 2022. Internal dynamics and metabolism of mercury in biota: a review of insights from mercury stable isotopes. Environ. Sci. Technol. 56 (13), 9182–9195.
Lin, H.M., Tong, Y.D., Yin, X.F., Zhang, Q.G., Zhang, H., Zhang, H.R., Chen, L., Kang, S. C., Zhang, W., Schauer, J., de Foy, B., Bu, X.G., Wang, X.J., 2019. First measurement of atmospheric mercury species in Qomolangma Natural Nature Preserve, Tibetan Plateau, and evidence of transboundary pollutant invasion. Atmos. Chem. Phys. 19 (2), 1373–1391.
Liu, B., Keeler, G.J., Dvonch, J.T., Barres, J.A., Lynam, M.M., Marsik, F.J., Morgan, J.T., 2007. Temporal variability of mercury speciation in urban air. Atmos. Environ. 41 (9), 1911–1923.
Liu, N., Qiu, G.G., Landis, M.S., Feng, X.B., Fu, X.W., Shang, L.H., 2011. Atmospheric mercury species measured in Guiyang, Guizhou province, Southwest China. Atmos. Res. 100 (1), 93–102.
Liu, C., Fu, X.W., Zhang, H., Ming, L.L., Xu, H., Zhang, L.M., Feng, X.B., 2019a. Sources and outflows of atmospheric mercury at Mt. Changbai, northeastern China. Sci. Total Environ. 663, 275–284.
Liu, H.-W., Shao, J.-J., Yu, B., Liang, Y., Duo, B., Fu, J.-J., Yang, R.-Q., Shi, J.-B., Jiang, G.-B., 2019b. Mercury isotopic compositions of mosses, conifer needles, and surface soils: Implications for mercury distribution and sources in Shergyla Mountain, Tibetan Plateau. Ecotoxicol. Environ. Saf. 172, 225–231.
Liu, K.Y., Wu, Q.R., Wang, L., Wang, S.X., Liu, T.H., Ding, D., Tang, Y., Li, G.L., Tian, H. Z., Duan, L., Wang, X., Fu, X.W., Feng, X.B., Hao, J.M., 2019c. Measure-specific

effectiveness of air pollution control on China's atmospheric mercury concentration and deposition during 2013-2017. Environ. Sci. Technol. 53 (15), 8938–8946.
Liu, C., Fu, X., Xu, Y., Zhang, H., Wu, X., Sommar, J., Zhang, L., Wang, X., Feng, X., 2022a. Sources and transformation mechanisms of atmospheric particulate bound mercury revealed by mercury stable isotopes. Environ. Sci. Technol. 56 (8), 5224–5233.
Liu, Y., Tian, J.W., Zheng, W.F., Yin, L.R., 2022b. Spatial and temporal distribution characteristics of haze and pollution particles in China based on spatial statistics. Urban Clim. 41.
Luo, H., Guan, Q., Shao, W., Du, Q., Xiao, X., Ni, F., Zhang, J., 2022. Quantifying the contribution of dust sources in the arid area of Northwest China using multivariate statistical techniques and Bayesian mixing models. J. Clean. Prod. 379, 134672.
Mao, H.T., Cheng, I., Zhang, L.M., 2016. Current understanding of the driving mechanisms for spatiotemporal variations of atmospheric speciated mercury: a review. Atmos. Chem. Phys. 16 (20), 12897–12924.
Mardani, A., Kannan, D., Hooker, R.E., Ozkul, S., Alrasheedi, M., Tirkolaee, E.B., 2020. Evaluation of green and sustainable supply chain management using structural equation modelling: A systematic review of the state of the art literature and recommendations for future research. J. Clean. Prod. 249.
Mil-Homens, M., Blum, J., Canário, J., Caetano, M., Costa, A.M., Lebreiro, S.M., Trancoso, M., Richter, T., de Stigter, H., Johnson, M., Branco, V., Cesário, R., Mouro, F., Mateus, M., Boer, W., Melo, Z., 2013. Tracing anthropogenic Hg and Pb input using stable Hg and Pb isotope ratios in sediments of the central Portuguese margin. Chem. Geol. 336, 62–71.
Moore, J.W., Semmens, B.X., 2008. Incorporating uncertainty and prior information into stable isotope mixing models. Ecol. Lett. 11 (5), 470–480.
Nair, U.S., Wu, Y., Walters, J., Jansen, J., Edgerton, E.S., 2012. Diurnal and seasonal variation of mercury species at coastal-suburban, urban, and rural sites in the southeastern United States. Atmos. Environ. 47, 499–508.
Nguyen, D.L., Kim, J.Y., Shim, S.-G., Zhang, X.-S., 2011. Ground and shipboard measurements of atmospheric gaseous elemental mercury over the Yellow Sea region during 2007–2008. Atmos. Environ. 45 (1), 253–260.
Nie, X.L., Wang, Y., Mao, H.T., Wang, T.J., Li, T., Wu, Y., Li, Y.X., Hou, C.X., Qie, G.H., Feng, X., Shang, Z.H., He, H.F., 2020. Atmospheric mercury in an eastern Chinese metropolis (Jinan). Ecotoxicol. Environ. Saf. 196, 110541.
Obrist, D., Kirk, J.L., Zhang, L., Sunderland, E.M., Jiskra, M., Selin, N.E., 2018. A review of global environmental mercury processes in response to human and natural perturbations: changes of emissions, climate, and land use. Ambio 47 (2), 116–140.
Pedregosa, F., Varoquaux, G., Gramfort, A., Michel, V., Thirion, B., Grisel, O., Blondel, M., Prettenhofer, P., Weiss, R., Dubourg, V., Vanderplas, J., Passos, A., Cournapeau, D., Brucher, M., Perrot, M., Duchesnay, É., 2011. Scikit-learn: machine learning in python. J. Mach. Learn. Res. 2825–2830, 12pp.
Perrot, V., Jimenez-Moreno, M., Berail, S., Epov, V.N., Monperrus, M., Amouroux, D., 2013. Successive methylation and demethylation of methylated mercury species (MeHg and DMeHg) induce mass dependent fractionation of mercury isotopes. Chem. Geol. 355, 153–162.
Poissant, L., Pilote, M., Beauvais, C., Constant, P., Zhang, H., 2005. A year of continuous measurements of three atmospheric mercury species (GEM, RGM and Hg) in southern Quebec, Canada. Atmos. Environ. 39 (7), 1275–1287.
Qin, X.F., Wang, F.W., Deng, C.R., Wang, F.J., Yu, G.Y., 2016. Seasonal variation of atmospheric particulate mercury over the East China Sea, an outflow region of anthropogenic pollutants to the open Pacific Ocean. Atmos. Pollut. Res. 7 (5), 876–883.
Qin, X.F., Wang, X.H., Shi, Y.J., Yu, G.Y., Zhao, N., Lin, Y.F., Fu, Q.Y., Wang, D.F., Xie, Z. Q., Deng, C.R., Huang, K., 2019. Characteristics of atmospheric mercury in a suburban area of East China: sources, formation mechanisms, and regional transport. Atmos. Chem. Phys. 19 (9), 5923–5940.
Qin, X., Dong, X., Tao, Z., Wei, R., Zhang, H., Guo, Q., 2023. Tracing the transboundary transport of atmospheric Particulate Bound Mercury driven by the East Asian monsoon. J. Hazard. Mater. 446, 130678.
Qiu, Y., Gai, P.X., Yue, F.E., Zhang, Y.Y., He, P.Z., Kang, H., Yu, X.W., Lam, P.K.S., Chen, J.B., Xie, Z.Q., 2021. Identification of potential sources of elevated PM2.5-Hg using mercury isotopes during haze events. Atmos. Environ. 247, 118203.
Rose, C.H., Ghosh, S., Blum, J.D., Bergquist, B.A., 2015. Effects of ultraviolet radiation on mercury isotope fractionation during photo-reduction for inorganic and organic mercury species. Chem. Geol. 405, 102–111.
Rosseel, Y., 2012. Lavaan: an R package for structural equation modeling. J. Stat. Softw. 48 (2), 1–36.
Rothenberg, S.E., Yin, R., Hurley, J.P., Krabbenhoft, D.P., Ismawati, Y., Hong, C., Donohue, A., 2017. Stable mercury isotopes in polished rice (Oryza sativa L.) and hair from rice consumers. Environ. Sci. Technol. 51 (11), 6480–6488.
Rutter, A.P., Schauer, J.J., 2007. The effect of temperature on the gas-particle partitioning of reactive mercury in atmospheric aerosols. Atmos. Environ. 41 (38), 8647–8657.
Schleicher, N.J., Schafer, J., Blanc, G., Chen, Y., Chai, F., Cen, K., Norra, S., 2015. Atmospheric particulate mercury in the megacity Beijing: Spatiotemporal variations and source apportionment. Atmos. Environ. 109, 251–261.
Schleicher, N.J., Schafer, J., Chen, Y., Blanc, G., Chen, Y., Chai, F., Cen, K., Norra, S., 2016. Atmospheric particulate mercury in the megacity Beijing: Efficiency of mitigation measures and assessment of health effects. Atmos. Environ. 124, 396–403.
Selin, N.E., Jacob, D.J., Park, R.J., Yantosca, R.M., Strode, S., Jaegle, L., Jaffe, D., 2007. Chemical cycling and deposition of atmospheric mercury: Global constraints from observations. J. Geophys. Res.-Atmos. 112 (D2).
Sherman, L.S., Blum, J.D., Johnson, K.P., Keeler, G.J., Barres, J.A., Douglas, T.A., 2010. Mass-independent fractionation of mercury isotopes in Arctic snow driven by sunlight. Nat. Geosci. 3 (3), 173–177.
Sherman, L.S., Blum, J.D., Keeler, G.J., Demers, J.D., Dvonch, J.T., 2012. Investigation of local mercury deposition from a coal-fired power plant using mercury isotopes. Environ. Sci. Technol. 46 (1), 382–390.
Sherman, L.S., Blum, J.D., Franzblau, A., Basu, N., 2013. New insight into biomarkers of human mercury exposure using naturally occurring mercury stable isotopes. Environ. Sci. Technol. 47 (7), 3403–3409.
Sherman, L.S., Blum, J.D., Basu, N., Rajaee, M., Evers, D.C., Buck, D.G., Petrlik, J., DiGangi, J., 2015. Assessment of mercury exposure among small-scale gold miners using mercury stable isotopes. Environ. Res. 137, 226–234.
Slemr, F., Brunke, E.G., Ebinghaus, R., Kuss, J., 2011. Worldwide trend of atmospheric mercury since 1995. Atmos. Chem. Phys. 11 (10), 4779–4787.
Smith, R.S., Wiederhold, J.G., Kretzschmar, R., 2015. Mercury isotope fractionation during precipitation of metacinnabar (beta-HgS) and montroydite (HgO). Environ. Sci. Technol. 49 (7), 4325–4334.
Sonke, J.E., Schafer, J., Chmeleff, J., Audry, S., Blanc, G., Dupre, B., 2010. Sedimentary mercury stable isotope records of atmospheric and riverine pollution from two major European heavy metal refineries. Chem. Geol. 279 (3–4), 90–100.
Sonke, J.E., Angot, H., Zhang, Y., Poulain, A., Björn, E., Schartup, A., 2023. Global change effects on biogeochemical mercury cycling. Ambio 52 (5), 853–876.
Sprovieri, F., Pirrone, N., Bencardino, M., D'Amore, F., Angot, H., Barbante, C., Brunke, E.G., Arcega-Cabrera, F., Cairns, W., Comero, S., Dieguez, M.D., Dommergue, A., Ebinghaus, R., Feng, X.B., Fu, X.W., Garcia, P.E., Gawlik, B.M., Hagestrom, U., Hansson, K., Horvat, M., Kotnik, J., Labuschagne, C., Magand, O., Martin, L., Mashyanov, N., Mkololo, T., Munthe, J., Obolkin, V., Islas, M.R., Sena, F., Somerset, V., Spandow, P., Varde, M., Walters, C., Wangberg, I., Weigelt, A., Yang, X., Zhang, H., 2017. Five-year records of mercury wet deposition flux at GMOS sites in the Northern and Southern hemispheres. Atmos. Chem. Phys. 17 (4), 2689–2708.
Steenhuisen, F., Wilson, S.J., 2019. Development and application of an updated geospatial distribution model for gridding 2015 global mercury emissions. Atmos. Environ. 211, 138–150.
Steffen, A., Bottenheim, J., Cole, A., Ebinghaus, R., Lawson, G., Leaitch, W.R., 2014. Atmospheric mercury speciation and mercury in snow over time at Alert, Canada. Atmos. Chem. Phys. 14 (5), 2219–2231.
Steffen, A., Lehnherr, I., Cole, A., Ariya, P., Dastoor, A., Durnford, D., Kirk, J., Pilote, M., 2015. Atmospheric mercury in the Canadian Arctic. Part I: A review of recent field measurements. Sci. Total Environ. 509-510, 3–15.
Stetson, S.J., Gray, J.E., Wanty, R.B., Macalady, D.L., 2009. Isotopic variability of mercury in ore, mine-waste calcine, and leachates of mine-waste calcine from areas mined for mercury. Environ. Sci. Technol. 43 (19), 7331–7336.
Stock, B.C., Jackson, A.L., Ward, E.J., Parnell, A.C., Phillips, D.L., Semmens, B.X., 2018. Analyzing mixing systems using a new generation of Bayesian tracer mixing models. PeerJ 6, e5096.
Streets, D.G., Devane, M.K., Lu, Z.F., Bond, T.C., Sunderland, E.M., Jacob, D.J., 2011. All-time releases of mercury to the atmosphere from human activities. Environ. Sci. Technol. 45 (24), 10485–10491.
Sun, R.Y., Heimburger, L.E., Sonke, J.E., Liu, G.J., Amouroux, D., Berail, S., 2013a. Mercury stable isotope fractionation in six utility boilers of two large coal-fired power plants. Chem. Geol. 336, 103–111.
Sun, Y., Wang, Z., Fu, P., Jiang, Q., Yang, T., Li, J., Ge, X., 2013b. The impact of relative humidity on aerosol composition and evolution processes during wintertime in Beijing, China. Atmos. Environ. 77, 927–934.
Sun, R., Sonke, J.E., Liu, G., Zheng, L., Wu, D., 2014a. Variations in the stable isotope composition of mercury in coal-bearing sequences: Indications for its provenance and geochemical processes. Int. J. Coal Geol. 133, 13–23.
Sun, R.Y., Sonke, J.E., Heimburger, L.E., Belkin, H.E., Liu, G.J., Shome, D., Cukrowska, E., Liousse, C., Pokrovsky, O.S., Streets, D.G., 2014b. Mercury stable isotope signatures of world coal deposits and historical coal combustion emissions. Environ. Sci. Technol. 48 (13), 7660–7668.
Sun, G.Y., Sommar, J., Feng, X.B., Lin, C.J., Ge, M.F., Wang, W.G., Yin, R.S., Fu, X.W., Shang, L.H., 2016a. Mass-dependent and -independent fractionation of mercury isotope during gas-phase oxidation of elemental mercury vapor by atomic Cl and Br. Environ. Sci. Technol. 50 (17), 9232–9241.
Sun, R.Y., Streets, D.G., Horowitz, H.M., Amos, H.M., Liu, G.J., Perrot, V., Toutain, J.P., Hintelmann, H., Sunderland, E.M., Sonke, J.E., 2016b. Historical (1850-2010) mercury stable isotope inventory from anthropogenic sources to the atmosphere. Elem. Sci. Anthrop. 4, 1–15.
Sun, G., Feng, X., Yang, C., Zhang, L., Yin, R., Li, Z., Bi, X., Wu, Y., 2020. Levels, sources, isotope signatures, and health risks of mercury in street dust across China. J. Hazard. Mater. 392, 122276.
Sun, L.M., Zhang, X.D., Zheng, J.Y., Zheng, Y.Q., Yuan, D.X., Chen, W.J., 2021. Mercury concentration and isotopic composition on different atmospheric particles (PM10 and PM2.5) in the subtropical coastal suburb of Xiamen Bay, Southern China. Atmos. Environ. 261, 118604.
Sun, R., Hintelmann, H., Wiklund, J.A., Evans, M.S., Muir, D., Kirk, J.L., 2022. Mercury isotope variations in lake sediment cores in response to direct mercury emissions from non-ferrous metal smelters and legacy mercury remobilization. Environ. Sci. Technol. 56 (12), 8266–8277.
Sunderland, E.M., 2007. Mercury exposure from domestic and imported Estuarine and marine fish in the U.S. Seafood Market. Environ. Health Perspect. 115 (2), 235–242.
Tang, S., Feng, C., Feng, X., Zhu, J., Sun, R., Fan, H., Wang, L., Li, R., Mao, T., Zhou, T., 2017. Stable isotope composition of mercury forms in flue gases from a typical coal-fired power plant, Inner Mongolia, northern China. J. Hazard. Mater. 328, 90–97.

Tang, Y., Wang, S.X., Wu, Q.R., Liu, K.Y., Wang, L., Li, S., Gao, W., Zhang, L., Zheng, H. T., Li, Z.J., Hao, J.M., 2018. Recent decrease trend of atmospheric mercury concentrations in East China: the influence of anthropogenic emissions. Atmos. Chem. Phys. 18 (11), 8279–8291.
Tang, Y., Wang, S.X., Wu, Q.R., Liu, K.Y., Li, Z.J., Zou, J., Hou, D.Y., Wu, Y., Duan, L., 2019. Measurement of size-fractionated particulate-bound mercury in Beijing and implications on sources and dry deposition of mercury. Sci. Total Environ. 675, 176–183.
Tang, X., Kong, L., Zhu, J., Wang, Z., Li, J., Wu, H., Wu, Q., Chen, H., Zhu, L., Wang, W., Liu, B., Wang, Q., Chen, D., Pan, Y., Song, T., Li, F., Zheng, H., Jia, G., Lu, M., Wu, L., Carmichael, G.R., 2021. A six-year long high-resolution air quality reanalysis dataset over China from 2013 to 2018 (monthly and annual version). Sci. Data Bank V2.
Tsui, M.T.-K., Blum, J.D., Finlay, J.C., Balogh, S.J., Nollet, Y.H., Palen, W.J., Power, M.E., 2014. Variation in terrestrial and aquatic sources of methylmercury in stream predators as revealed by stable mercury isotopes. Environ. Sci. Technol. 48 (17), 10128–10135.
Wang, Z.W., Zhang, X.S., Chen, Z.S., Zhang, Y., 2006. Mercury concentrations in size-fractionated airborne particles at urban and suburban sites in Beijing, China. Atmos. Environ. 40 (12), 2194–2201.
Wang, Z., Chen, J., Feng, X., Hintelmann, H., Yuan, S., Cai, H., Huang, Q., Wang, S., Wang, F., 2015. Mass-dependent and mass-independent fractionation of mercury isotopes in precipitation from Guiyang, SW China. Compt. Rendus Geosci. 347 (7–8), 358–367.
Wang, X., Luo, J., Yin, R.S., Yuan, W., Lin, C.J., Sommar, J., Feng, X.B., Wang, H.M., Lin, C., 2017. Using mercury isotopes to understand mercury accumulation in the Montane Forest Floor of the Eastern Tibetan Plateau. Environ. Sci. Technol. 51 (2), 801–809.
Wang, S., McNamara, S.M., Moore, C.W., Obrist, D., Steffen, A., Shepson, P.B., Staebler, R.M., Raso, A.R.W., Pratt, K.A., 2019. Direct detection of atmospheric atomic bromine leading to mercury and ozone depletion. Proc. Natl. Acad. Sci. 116 (29), 14479–14484.
Wang, C.J., Wang, Z.W., Zhang, X.S., 2020. Two years measurement of speciated atmospheric mercury in a typical area of the north coast of China: sources, temporal variations, and influence of regional and long-range transport. Atmos. Environ. 228, 117235.
Wang, C.J., Hui, F., Gao, Y., Wang, Z.W., Zhang, X.S., 2021a. Temporal variation of speciated atmospheric Hg and characteristics of size-fractioned Hg-P at a suburban site in Shijiazhuang City, North China. Atmos. Pollut. Res. 12 (12), 101253.
Wang, C.J., Wang, Z.W., Zhang, X.S., 2021b. Speciated atmospheric mercury during haze and non-haze periods in winter at an urban site in Beijing, China: Pollution characteristics, sources, and causes analyses. Atmos. Res. 247, 105209.
Wang, X., Yuan, W., Lin, C.J., Feng, X.B., 2021c. Mercury cycling and isotopic fractionation in global forests. Crit. Rev. Environ. Sci. Technol. 52 (21), 3763–3786.
Weigelt, A., Ebinghaus, R., Manning, A.J., Derwent, R.G., Simmonds, P.G., Spain, T.G., Jennings, S.G., Slemr, F., 2015. Analysis and interpretation of 18 years of mercury observations since 1996 at Mace Head, Ireland. Atmos. Environ. 100, 85–93.
Weiss-Penzias, P.S., Gay, D.A., Brigham, M.E., Parsons, M.T., Gustin, M.S., ter Schure, A., 2016. Trends in mercury wet deposition and mercury air concentrations across the US and Canada. Sci. Total Environ. 568, 546–556.
Wiederhold, J.G., Smith, R.S., Siebner, H., Jew, A.D., Brown Jr., G.E., Bourdon, B., Kretzschmar, R., 2013. Mercury isotope signatures as tracers for Hg cycling at the New Idria Hg mine. Environ. Sci. Technol. 47 (12), 6137–6145.
Wu, Q., Wang, S., Li, G., Liang, S., Lin, C.J., Wang, Y., Cai, S., Liu, K., Hao, J., 2016. Temporal trend and spatial distribution of speciated atmospheric mercury emissions in China during 1978-2014. Environ. Sci. Technol. 50 (24), 13428–13435.
Xia, J., Wang, J., Zhang, L., Wang, X., Yuan, W., Peng, T., Zheng, L., Tian, W., Feng, X., 2022. Migration and transformation of soil mercury in a karst region of southwest China: Implications for groundwater contamination. Water Res. 226, 119271.
Xia, J., Wang, J., Zhang, L., Wang, X., Yuan, W., Peng, T., Zheng, L., Tian, W., Feng, X., 2022. Migration and transformation of soil mercury in a karst region of southwest China: Implications for groundwater contamination. Water Res 226, 119271.
Xiong, B., Skitmore, M., Xia, B., 2015. A critical review of structural equation modeling applications in construction research. Autom. Constr. 49, 59–70.
Xiu, G.L., Cai, J., Zhang, W.Y., Zhang, D.N., Bueler, A., Lee, S.C., Shen, Y., Xu, L.H., Huang, X.J., Zhang, P., 2009. Speciated mercury in size-fractionated particles in Shanghai ambient air. Atmos. Environ. 43 (19), 3145–3154.
Xu, L.L., Chen, J.S., Yang, L.M., Niu, Z.C., Tong, L., Yin, L.Q., Chen, Y.T., 2015. Characteristics and sources of atmospheric mercury speciation in a coastal city, Xiamen, China. Chemosphere 119, 530–539.
Xu, H.M., Sonke, J.E., Guinot, B., Fu, X.W., Sun, R.Y., Lanzanova, A., Candaudap, F., Shen, Z.X., Cao, J.J., 2017. Seasonal and annual variations in atmospheric Hg and Pb isotopes in Xi'an, China. Environ. Sci. Technol. 51 (7), 3759–3766.
Xu, H.M., Sun, R.Y., Cao, J.J., Huang, R.J., Guinot, B., Shen, Z.X., Jiskra, M., Li, C.X., Du, B.Y., He, C., Liu, S.X., Zhang, T., Sonke, J.E., 2019. Mercury stable isotope compositions of Chinese urban fine particulates in winter haze days: Implications for Hg sources and transformations. Chem. Geol. 504, 267–275.
Xu, L.L., Zhang, Y.R., Tong, L., Chen, Y.P., Zhao, G.Q., Hong, Y.W., Xiao, H., Chen, J.S., 2020. Gas-particle partitioning of atmospheric reactive mercury and its contribution to particle bound mercury in a coastal city of the Yangtze River Delta, China. Atmos. Environ. 239, 117744.
Xu, L.L., Shi, J.Y., Chen, Y.P., Zhang, Y.R., Yang, M.R., Chen, Y.T., Yin, L.Q., Tong, L., Xiao, H., Chen, J.S., 2021. Mercury isotopic compositions in fine particles and offshore surface seawater in a coastal area of East China: implications for Hg sources and atmospheric transformations. Atmos. Chem. Phys. 21 (24), 18543–18555.
Yang, H.D., Engstrom, D.R., Rose, N.L., 2010. Recent changes in atmospheric mercury deposition recorded in the sediments of remote equatorial lakes in the Rwenzori Mountains, Uganda. Environ. Sci. Technol. 44 (17), 6570–6575.
Yang, S., Wang, B., Qin, C., Yin, R., Li, P., Liu, J., Point, D., Maurice, L., Sonke, J.E., Zhang, L., 2021. Compound-specific stable isotope analysis provides new insights for tracking human monomethylmercury exposure sources. Environ. Sci. Technol. 55 (18), 12493–12503.
Yang, Y.H., Kwon, S.Y., Tsui, M.T.-K., Motta, L.C., Washburn, S.J., Park, J., Kim, M.-S., Shin, K.-H., 2022. Ecological traits of fish for mercury biomonitoring: insights from compound-specific nitrogen and stable mercury isotopes. Environ. Sci. Technol. 56 (15), 10808–10817.
Ye, Z., Mao, H., Lin, C.-J., Kim, S.Y., 2016. Investigation of processes controlling summertime gaseous elemental mercury oxidation at midlatitudinal marine, coastal, and inland sites. Atmos. Chem. Phys. 16 (13), 8461–8478.
Yin, R., Feng, X., Meng, B., 2013a. Stable mercury isotope variation in rice plants (Oryza sativa L.) from the Wanshan mercury mining district, SW China. Environ. Sci. Technol. 47 (5), 2238–2245.
Yin, R., Feng, X., Wang, J., Bao, Z., Yu, B., Chen, J., 2013b. Mercury isotope variations between bioavailable mercury fractions and total mercury in mercury contaminated soil in Wanshan Mercury Mine, SW China. Chem. Geol. 336, 80–86.
Yin, R., Feng, X., Wang, J., Li, P., Liu, J., Zhang, Y., Chen, J., Zheng, L., Hu, T., 2013c. Mercury speciation and mercury isotope fractionation during ore roasting process and their implication to source identification of downstream sediment in the Wanshan mercury mining area, SW China. Chem. Geol. 336, 72–79.
Yin, R., Feng, X., Chen, J., 2014a. Mercury stable isotopic compositions in coals from major coal producing fields in china and their geochemical and environmental implications. Environ. Sci. Technol. 48 (10), 5565–5574.
Yin, R., Feng, X., Li, X., Yu, B., Du, B., 2014b. Trends and advances in mercury stable isotopes as a geochemical tracer. Trends Environ. Anal. Chem. 2, 1–10.
Yin, R., Feng, X., Chen, B., Zhang, J., Wang, W., Li, X., 2015. Identifying the sources and processes of mercury in subtropical estuarine and ocean sediments using Hg isotopic composition. Environ. Sci. Technol. 49 (3), 1347–1355.
Yu, B., Fu, X.W., Yin, R.S., Zhang, H., Wang, X., Lin, C.J., Wu, C.S., Zhang, Y.P., He, N.N., Fu, P.Q., Wang, Z.F., Shang, L.H., Sommar, J., Sonke, J.E., Maurice, L., Guinot, B., Feng, X.B., 2016. Isotopic composition of atmospheric mercury in China: new evidence for sources and transformation processes in air and in vegetation. Environ. Sci. Technol. 50 (17), 9262–9269.
Yu, G.Y., Qin, X.F., Xu, J., Zhou, Q., Wang, B., Huang, K., Deng, C.R., 2019. Characteristics of particulate-bound mercury at typical sites situated on dust transport paths in China. Sci. Total Environ. 648, 1151–1160.
Yu, B., Yang, L., Liu, H., Xiao, C., Bu, D., Zhang, Q., Fu, J., Zhang, Q., Cong, Z., Liang, Y., Hu, L., Yin, Y., Shi, J., Jiang, G., 2022. Tracing the transboundary transport of mercury to the Tibetan Plateau using atmospheric mercury isotopes. Environ. Sci. Technol. 56 (3), 1568–1577.
Yuan, C.S., Jhang, Y.M., Ie, I.R., Lee, C.E., Fang, G.C., Luo, J.J., 2021. Exploratory investigation on spatiotemporal variation and source identification of atmospheric speciated mercury surrounding the Taiwan Strait. Atmos. Pollut. Res. 12 (3), 54–64.
Yuan, S., Chen, J., Hintelmann, H., Cai, H., Yuan, W., He, S., Zhang, K., Zhang, Y., Liu, Y., 2022a. Event-based atmospheric precipitation uncovers significant even and odd Hg isotope anomalies associated with the circumpolar vortex. Environ. Sci. Technol. 56 (17), 12713–12722.
Yuan, W., Wang, X., Lin, C.-J., Wu, F., Luo, K., Zhang, H., Lu, Z., Feng, X., 2022b. Mercury uptake, accumulation, and translocation in roots of subtropical forest: implications of global mercury budget. Environ. Sci. Technol. 56 (19), 14154–14165.
Zhang, F., Xu, L., Chen, J., Yu, Y., Niu, Z., Yin, L., 2012. Chemical compositions and extinction coefficients of PM2. 5 in peri-urban of Xiamen, China, during June 2009–May 2010. Atmos. Res. 106, 150–158.
Zhang, H., Fu, X.W., Lin, C.J., Wang, X., Feng, X.B., 2015. Observation and analysis of speciated atmospheric mercury in Shangri-La, Tibetan Plateau, China. Atmos. Chem. Phys. 15 (2), 653–665.
Zhang, Y.X., Jacob, D.J., Horowitz, H.M., Chen, L., Amos, H.M., Krabbenhoft, D.P., Slemr, F., St Louis, V.L., Sunderland, E.M., 2016. Observed decrease in atmospheric mercury explained by global decline in anthropogenic emissions. Proc. Natl. Acad. Sci. U. S. A. 113 (3), 526–531.
Zhang, L., Wang, L., Wang, S.X., Dou, H.Y., Li, J.F., Li, S., Hao, J.M., 2017. Characteristics and sources of speciated atmospheric mercury at a coastal site in the East China Sea Region. Aerosol Air Qual. Res. 17 (12), 2913–2923.
Zhang, H., Wang, Z.W., Wang, C.J., Zhang, X.S., 2019. Concentrations and gas-particle partitioning of atmospheric reactive mercury at an urban site in Beijing, China. Environ. Pollut. 249, 13–23.
Zhang, H., Fu, X.W., Yu, B., Li, B.X., Liu, P., Zhang, G.Q., Zhang, L.M., Feng, X.B., 2021a. Speciated atmospheric mercury at the Waliguan Global Atmosphere Watch station in the northeastern Tibetan Plateau: implication of dust-related sources for particulate bound mercury. Atmos. Chem. Phys. 21 (20), 15847–15859.
Zhang, L., Zhou, P.S., Zhong, H., Zhao, Y., Dai, L., Wang, Q.G., Xi, M.X., Lu, Y., Wang, Y. T., 2021b. Quantifying the impacts of anthropogenic and natural perturbations on gaseous elemental mercury (GEM) at a suburban site in eastern China using generalized additive models. Atmos. Environ. 247.
Zhang, K., Zheng, W., Sun, R., He, S., Shuai, W., Fan, X., Yuan, S., Fu, P., Deng, J., Li, X., Wang, S., Chen, J., 2022. Stable Isotopes Reveal Photoreduction of Particle-Bound Mercury Driven by Water-Soluble Organic Carbon during Severe Haze. Environ. Sci. Technol. 56 (15), 10619–10628.
Zhang, Y., Zhang, L., Cao, S., Liu, X., Jin, J., Zhao, Y., 2023. Improved anthropogenic mercury emission inventories for China from 1980 to 2020: toward more accurate

effectiveness evaluation for the minamata convention. Environ. Sci. Technol. 57 (23), 8660–8670.
Zheng, W., Hintelmann, H., 2009. Mercury isotope fractionation during photoreduction in natural water is controlled by its Hg/DOC ratio. Geochim. Cosmochim. Acta 73 (22), 6704–6715.
Zheng, W., Obrist, D., Weis, D., Bergquist, B.A., 2016. Mercury isotope compositions across north American forests. Glob. Biogeochem. Cycles 30 (10), 1475–1492.
Zheng, W., Demers, J.D., Lu, X., Bergquist, B.A., Anbar, A.D., Blum, J.D., Gu, B., 2019. Mercury stable isotope fractionation during abiotic dark oxidation in the presence of thiols and natural organic matter. Environ. Sci. Technol. 53 (4), 1853–1862.
Zheng, W., Chandan, P., Steffen, A., Stupple, G., De Vera, J., Mitchell, C.P.J., Wania, F., Bergquist, B.A., 2021. Mercury stable isotopes reveal the sources and transformations of atmospheric Hg in the high Arctic. Appl. Geochem. 131, 105002.
Zhu, J., Wang, T., Talbot, R., Mao, H., Yang, X., Fu, C., Sun, J., Zhuang, B., Li, S., Han, Y., Xie, M., 2014. Characteristics of atmospheric mercury deposition and size-fractionated particulate mercury in urban Nanjing, China. Atmos. Chem. Phys. 14 (5), 2233–2244.